Introduction to dissolution DNP: Overview, instrumentation, and human applications

Ardenkjær-Larsen, Jan Henrik

Published in:
eMagRes

Link to article, DOI:
10.1002/9780470034590.emrstm1549

Publication date:
2018

Document Version
Peer reviewed version

Introduction to Dissolution DNP: Overview, Instrumentation & Human Applications

Jan H. Ardenkjaer-Larsen[1,2]

[1]Technical University of Denmark, Department of Electrical Engineering, Center for Magnetic Resonance, 2800 Kgs Lyngby, Denmark, [2]GE Healthcare, 2650 Brøndby, Denmark

Corresponding address:

Jan Henrik Ardenkjaer-Larsen

Center for Magnetic Resonance

Department of Electrical Engineering

Ørsted Plads, bldg 349, office 126

2800 Kgs Lyngby

Denmark

Email: jhar@elektro.dtu.dk

Key Words: hyperpolarization, Dynamic Nuclear Polarization, dDNP, Magnetic Resonance

Words (7200 max):

Abstract

In this article, we describe the basic principles of dissolution dynamic nuclear polarization (dDNP). Hyperpolarization is a technique to enhance the nuclear polarization and thereby increase the available signal in Magnetic Resonance (MR). We will discuss the consequences of strong non-equilibrium nuclear spin polarization acquisition of the MR signal. The hardware requirements for clinical translation of this technology are presented. For studies that allow the use of externally administered agents, hyperpolarization offers a way to overcome normal magnetic resonance sensitivity limitations, at least for a brief T_1-dependent observation window. A 10,000 to 100,000-fold signal-to-noise advantage provides an avenue for real time measurement of perfusion, metabolite transport, exchange and metabolism. The principles behind these measurements, as well as the choice of agent, and progress toward the application of hyperpolarized ^{13}C metabolic imaging in oncology, cardiology and neurology are reviewed.

Introduction

The aim of this article is to introduce the basic principles and progress toward the clinical application of hyperpolarization using dissolution Dynamic Nuclear Polarization (dDNP). Less than a decade passed from first published [1] to first in man [2–5]. During this time a research field has emerged studying the basic physics of DNP, developing advanced dDNP instrumentation, optimizing acquisition hardware and pulse sequences, and applying the method to study a range of bioprobes in biological systems.

Hyperpolarization indicates that the polarization is no longer determined by the static magnetic field of the scanner. A polarizer enhances the polarization of the nuclear spins outside the imaging system. The hyperpolarization method can be based on several principles [6], of which, two have successfully been applied to molecules in solution: Para-Hydrogen Induced Polarization (PHIP) and dDNP. The dDNP method has been particularly successful in making solutions of biologically interesting molecules with highly polarized nuclear spins. The method takes advantage of DNP in the solid state followed by rapid dissolution in a suitable solvent. The dissolution step retains almost completely the nuclear spin polarization, creating a solution with a non-thermal nuclear polarization approaching unity.

Hyperpolarized Metabolic MR grew out of vision that MR as modality has excellent properties for studying the biochemical changes associated with disease, and that early diagnosis, staging and response monitoring required characterization of the disease at the cellular and biochemical level. The MR spectrum provides both identification and quantification of the metabolites involved. However, MR Spectroscopy (MRS) suffers from several limitations: poor sensitivity, leading to long scan-times and poor spatial resolution, and limited spectral resolution due to a crowded spectrum. The long scan time means that only steady-state concentrations or

slow dynamic changes can be measured. To overcome the tremendous challenge with sensitivity, hyperpolarization seemed the most powerful vista to take. The potential for 10,000-fold enhancement of nuclear spin polarization would compensate the low metabolite concentrations and enable otherwise impossible studies.

Dynamic Nuclear Polarization

DNP was first described theoretically by Overhauser in 1953 [7], and a few months later demonstrated by Carver and Slichter [8] in metallic lithium. Overhauser predicted that saturating the conduction electrons of a metal would lead to a dynamic polarization of the nuclear spins. This was a fundamental discovery causing disbelief at the time: that heating of one spin system could lead to the cooling of another. Abragam soon extended the prediction by Overhauser for metals to electron spins in solution [9], and most NMR spectroscopists are today familiar with the nuclear and electronic Overhauser effect. Relaxation processes that couple the spins via molecular motions drive this effect. Soon after, the Solid Effect was described for spins in the solid state coupled by dipolar interactions [10]. Later, DNP in the solid state was extended mechanistically to processes involving several electron spins [11]. The theory of DNP in the solid state, however, has failed to provide a quantitative description of the general case. However, the theoretical description of DNP has made significant progress in recent years. For a recent comprehensive description of DNP based on spin temperature concepts see [12–14]. In the solid state, microwave irradiation close to the resonance frequency of the electron spin transfer, in part, the high electron spin polarization to the nuclear spins. The efficiency of this process depends on several parameters characterizing the various spin systems, but also on technical factors such as microwave frequency and power.

Polarization is the difference in population between the two possible energy eigenstates for a spin ½, and is given by

$$P = \frac{N^+ - N^-}{N^+ + N^-} = \tanh\left(\frac{\gamma \hbar B_0}{2 k_B T}\right) \qquad [1]$$

where N^+ and N^- denote the number of spins parallel (spin up) and anti-parallel (spin down) to the external magnetic field, respectively. According to Eq. [1] a temperature can be assigned to the spins for any polarization. For example *P=0*, complete saturation, corresponds to an infinite spin temperature. Depending on the sign of the polarization, the spin temperature can be either negative or positive, and will approach zero (cooling) as the polarization approaches unity. As a point of caution, it is often stated that spins are either pointing up or down, i.e. is in one of the two eigenstates. However, this is not correct. Quoting Slichter [15]: "We emphasize that an arbitrary orientation can be specified, since sometimes the belief is erroneously held that spins may only be found pointing either parallel or antiparallel to the quantizing field. One of the beauties of quantum theory is that it contains features of both discreteness and continuity. In terms of the two quantum states with m=±½ we can describe an expectation value of the magnetization which goes all the way from parallel to antiparallel, including all values in between. …". The spin is therefore in a superposition of the eigenstates, and it is perfectly valid to speak of populations (probabilities) of the eigenstates. The proton polarization in a 3 T MR scanner becomes $10 \cdot 10^{-6}$, while the polarization for ^{13}C is only $2.5 \cdot 10^{-6}$. A theoretical enhancement of the polarization of 100,000 and 400,000 times, respectively, is therefore possible, if unity polarization could be achieved.

Electron paramagnetic agent (EPA)

DNP requires the presence of unpaired electrons, typically in the form of an organic radical, but a few metal ions have high efficiency for DNP at low temperature, Cr(V) in particular. The magnetic moment of the electron is 658 times higher than that of the proton. This means that the electron spin will reach unity polarization at a moderate magnetic field strength and liquid helium temperature, Fig 1. At e.g. 3.35 T and 1 K the electron spin polarization is already 98%. The choice of EPA will depend on a number of factors. Firstly, the EPA needs to be chemically stable and dissolve readily in the matrix of interest. Secondly, the electron paramagnetic resonance (EPR) spectrum of the radical should have a width that allows DNP to be effective for the nucleus of interest, i.e. a line width that exceeds the Larmor frequency of the nuclear spin. Thirdly, the EPA should have low toxicity and, ideally, be removable from the hyperpolarized solution. In practice the above criteria mean that two classes of EPA are available, namely nitroxides and trityls [16,17]. The nitroxides belong to a class of molecules that have been studied extensively by EPR, and which have been used for DNP for many samples. Nitroxides are characterized by having a broad EPR spectrum. The EPR line width is approx. 4.0 promille (‰) of the EPR frequency, compared to the ^{1}H resonance frequency, which is 1.5 ‰ of the EPR frequency. Some of them have reasonable chemical stability and come with different degrees of hydrophilicity. The trityl is another class of EPA with superior properties for direct polarization of low gamma nuclei such as ^{13}C, ^{15}N and ^{2}H. These radicals have a line width that is only approx. 0.80 ‰ of the resonance frequency, much less than the proton resonance frequency, but perfectly matched for ^{13}C, which has a resonance frequency, which is 0.37 ‰ of the EPR frequency. The trityls exist with a range of hydrophilicities, and they are typically very stable chemically.

It has been shown that a small amount of gadolinium can positively affect the DNP enhancement in the solid [18]. Other paramagnetic ions and molecules (Mn^{2+} and O_2) can in part have the same effect. A shortening of the EPA relaxation times can explain the effect. Adding 1-2 mmol/L chelated Gd^{3+} leads to a 50-100% improvement of the DNP enhancement factor for pyruvic acid. The effect seems to be general to most samples, but each sample has to be optimized similarly to the concentration of the EPA. There is no direct DNP effect of the Gd^{3+} by itself under the conditions typically used (almost unity polarization of the EPA). Finally, Gd^{3+} may enhance the solid-state polarization by DNP, but care should be taken in avoiding accelerated relaxation in the liquid state. Free Gd ions would cause detrimental liquid state relaxation and pose an *in vivo* safety risk. After dissolution, the low concentration of radical and chelated Gd will have negligible effect on T_1 in most cases.

A new class of EPA, with wider prospects, is UV-generated radicals [19]. A precursor molecule, e.g. pyruvic acid itself, can be excited with UV light to produce a radical species with good ESR properties for DNP. The radical is labile and has to be generated at low temperature, e.g. 77 K. In the dissolution process the radical annihilates and decomposes into acetate and bicarbonate. However, the most exciting prospect for these radicals, is the potential for generating radical-free, hyperpolarized solids that can be transported over longer distances (see instrumentation section).

Imaging agents

A key limitation of the method is the short life time of hyperpolarization. Long longitudinal relaxation times, T_1, of tens of seconds to minutes can be found for ^{13}C that have no

directly attached protons, such as carboxylic acids or carbonyls. An example is pyruvate enriched with ^{13}C in either the C-1 or C-2 positions, both having a T_1 of about 60 s. It is also possible to obtain sufficiently long T_1 by deuteration of directly attached protons, as in e.g. [U-^{13}C,U-^{2}H]glucose, however, in this case, obtaining a T_1 of only approx. 20 s. Therefore, the imaging agent, or bioprobe, has to target metabolic pathways that has high uptake and metabolic rates on the time scale of T_1.

Another requirement for the imaging agent is that product and substrates have chemical shifts that are well separated to resolve the different metabolites. Chemical shift values for many in vivo metabolites can be found at the homepage of the Advanced Imaging Research Center, UTSouthwestern Medical Center (https://www.utsouthwestern.edu/education/medical-school/departments/airc/tools-references/chemical-shifts/).

Of the growing list of agents investigated *in vivo* using this method (Table 1, for a more comprehensive list see [20]), the most studied is [1-^{13}C]pyruvate. Pyruvate can be reduced to lactate, transaminated to alanine, or will lose the C-1 carbon as $^{13}CO_2$ when entering the Krebs cycle. This agent has shown great utility in oncology, as exemplified by the many studies summarized later in this chapter. [1-^{13}C]pyruvate was also the first agent to be used in a human study of hyperpolarized metabolic imaging [2]. Many of the most promising agents are reviewed in relation to the different applications of dDNP.

DNP sample preparation

The first step in hyperpolarizing a new imaging agent by dDNP is to find a formulation with high concentration the agent, and good solubility of the EPA. In order for the DNP process

to be effective, the EPA must be homogeneously distributed within the sample. Many molecules will be crystalline, or have a tendency to crystallize as saturated aqueous solutions. This will cause the EPA to concentrate in domains and lead to poor a DNP effect. To prevent this, the sample should stay amorphous when frozen to ensure homogenous distribution of the EPA. Three examples of molecules that are liquids at room temperature and stay amorphous when frozen without additives are [1-^{13}C]pyruvic acid (or any other isotopic labeling), 2-keto-[1-^{13}C]isocaproic acid and *bis*-1,1-(hydroxymethyl)-[1-^{13}C]cyclopropane-d_8 (HP001). All three molecules are liquids at room temperature and dissolve well a hydrophilic EPA.

For other compounds, it is necessary to prevent crystallization by mixing or dissolving the compound in a suitable solvent such as glycerol or dimethylsulfoxide (DMSO) can be used as solvent for the molecule and the EPA. For *in vivo* studies, it is necessary to formulate the molecule in a concentrated form in order to achieve a high concentration of the molecule after dissolution. To give an estimate of the requirements, a patient dose of 0.1 mmol/kg body weight can be assumed for an imaging agent with low toxicity, requiring approximately 10 mmol of compound. This means approx. 1 g of imaging agent, assuming a molecular weight of 100 g/mol. To keep the sample size reasonable requires a solubility of 30-50%. A solvent mixture with high solubility for the molecule and EPA, preventing sample crystallization and with good *in vivo* tolerance therefore has to be chosen. An example of a biologically compatible formulation is fumaric acid (e.g. [1,4-$^{13}C_2$, 2,3-D_2]fumaric acid) in DMSO. DMSO is a widely used solvent for pharmaceuticals and has a good safety profile. As a saturated solution of fumaric acid with a molarity of 3.6 mol/L or 1:1.8 (w:w), the solution forms an amorphous solid when frozen, if the cooling rate is not too slow. Dry DMSO should be used as small amounts of water will decrease solubility and increase supersaturation.

Another means of improving the solubility involves changing the counter ion of salts. Solubility typically increases with increasing size of the counter ion, and two examples of this can be mentioned: The cesium salt of bicarbonate, $CsH^{13}CO_3$, and the TRIS salt of acetate [21]. Both of these salts have higher solubility than their sodium counterpart. Finally, for amino acids (zwitter ions at neutral pH) it has shown that either high or low pH preparations increase the aqueous solubility by reducing the charge of the molecule to a point [21] that no or little glycerol is needed to form an amorphous sample.

Finally, Ji et al [22] showed that microcrystals of solids can be polarized by impregnation with a water:glycerol solution of a nitroxide. The proton polarization of the microcrystals is enhanced by spin diffusion from the impregnation. However, reduced polarization and longer polarization time is observed.

Formulations for many of the most used imaging agents can be found on the homepage of the Hyperpolarized MRI Technology Resource Center at UCSF (https://radiology.ucsf.edu/research/labs/hyperpolarized-mri-tech/training).

Dissolution and relaxation in the liquid state

To make the polarized solid sample useful for *in vivo* imaging, the sample is dissolved in a suitable buffer. Depending on the DNP sample, the dissolution may involve neutralization of the agent with acid or base. Buffering of the solution may be required to maintain control of pH within the physiologic range of 6.8 to 8.1. Physiological buffers such as tris(hydroxymethyl)aminomethane(TRIS) or 4-(2-hydroxyethyl)piperazine-1-ethanesulfonate (HEPES) are commonly used. An isotonic formulation is desired. This may mean lowering the

concentration of the imaging agent, if it is hypertonic, or adding sodium chloride if hypotonic. The dissolution has to be efficient and fast compared to the nuclear T_1 in order to preserve the nuclear polarization during the phase transition. Formulating the solid sample as beads or powder may improve the dissolution in terms of polarization loss and recovery of the imaging agent. Optimizing the fluid dynamics as well as providing the necessary heat is essential for optimal performance of more difficult agents [23]. To minimize relaxation, dissolution is performed inside the cryostat in the high field of the polarizer (e.g. ~3 T in the case of a 3.35 T polarizer), but above the liquid helium surface. As an example, the T_1 of the C-1 of [1-^{13}C]pyruvic acid at 9.4 T is ~1.6 s at 0 °C (unpublished data), and is attributed to dipolar relaxation by the solvent and methyl protons. According to theory, the minimum T_1 scales with B_0, which means that a minimum T_1 of 0.7 s should be expected during the dissolution in the 3 T polarizer field. Dissolution should happen on a faster time scale to avoid a loss of polarization. The severity of the problem will depend on the target spin and sample properties, but several parameters can be controlled, e.g. distances to other spins (labeling position), the abundance of other spins (full or partial deuteration, as well of the solvent) and the concentration of the EPA.

Any paramagnetic impurities that could increase the relaxation rate can be chelated by adding, for example, ethylenedinitrotetraacetic acid (EDTA) to the dissolution solvent. In most cases, the EPA or Gd chelate do not cause significant relaxation after dissolution and may be safe to inject into animals. For pre-clinical imaging it is not required to remove the EPA. The same applies to the Gd chelate in case it is used in the formulation. However, the solution may undergo a filtration or chromatography step to remove the EPA involved in the DNP process. In case a Gd chelate has been added, this agent may be removed as well. The filtration can either be in-line with the dissolution process or a subsequent step. In either case, the filtration is completed

in a matter of a few seconds with insignificant loss of polarization or target molecule. As an example, in the case of clinical studies with pyruvate, the solid sample is neat pyruvic acid (^{13}C-labelled) with 15 mM trityl radical (AH111501). The solid sample is dissolved in water-for-injection, which causes the trityl to precipitate under the acidic conditions. The solid EPA is then removed by filtration, and the pyruvic acid is neutralized post dissolution.

dDNP instrumentation

It is important to choose magnetic field and temperature conditions for DNP that lead to high nuclear polarization, but at the same time are easily achievable. Temperatures of ~1 K can be achieved by pumping on liquid helium. In the original dDNP polarizer design the liquid helium was supplied to the sample space through a needle valve from the magnet cryostat, but an alternative design has used a separate helium dewar [24]. In both cases, the low temperature is achieved with large mechanical pumps (200-500 m^3/h) that vent the gas to atmosphere. This makes the helium consumption and running costs high. The first polarizer had a magnetic field strength of 3.35 T, since microwave sources are readily available at 94 GHz for irradiation of the electron spin. The microwave power is guided to the sample through oversized waveguide in stainless steel to reduce thermal heat loads. Similarly, the NMR probe is constructed with stainless steel coaxial cable. To ensure that the sample is effectively cooled, it is typically immersed in liquid helium. The gas phase does not provide sufficient thermal conductivity (vapor pressure of 1 mbar at 1.2 K). The sample is loaded in a cup that is immersed in the helium bath. At dissolution the sample is raised out of the helium bath, but stays within the magnetic field, and a dissolution stick is introduced quickly and seals with the sample cup before the superheated solvent is injected at a typical pressure of 10 bar (water vapor pressure at 180 °C).

The latent heat of an organic sample is typically 500-1000 J/g, and this energy is easily provided by the superheated solvent (4.2 J/K/g). By proper design of the dissolution system, low dilution factors can be obtained [25].

At a temperature of app 1 K, the electron T_1, T_{1e}, is in the range of 0.1-1 s. The EPR line is effectively homogeneous at the concentrations used for DNP, and the resonant absorption for complete saturation can be estimated as $P = \gamma hbarN/2T_{1e}$, which for 15 mM electron spins and T_{1e} of 1 s is equal to 0.5 mW/cm^3. For shorter relaxation time and higher spin concentration, more MW power is needed, but the required power is relatively modest for low temperature DNP. Nitroxides are inhomogeneously broadened and microwave modulation is beneficial to efficiently saturate the EPR line [26].

A DNP polarizer designed with sterile use intent [27] was published with these main features

1. To provide a sterile barrier to the product through a single use fluid path.
2. To eliminate consumption of liquid cryogens.
3. To increase throughput by having four independent parallel samples.
4. To increase the size of the individual DNP samples up to 2.0 mL.
5. To automate the operation and remove operator variability and interventions.
6. To add Quality Control (QC).

The polarizer (SPINlab, GE Healthcare) operates at 5 T and 0.9 K in a closed cycle operation. There is no loss of cryogens in the operation. The cryostat consists of a superconducting magnet with liquid helium, but the cooling power is provided by a cryocooler.

The sample cooling is provided by a sorption pump, which is a canister filled with 7 kg of charcoal that will adsorb helium when cooled and releases the helium gas again when heated. The charcoal is cooled by closing a thermal switch connecting the sorption pump to the cryo-cooler driving the temperature of the charcoal to 5-6 K. The helium gas adsorbs, the pressure drops and the helium bath temperature drops. This can continue until the charcoal saturates and the helium bath runs dry. The adsorbed helium can then be regenerated by opening the thermal switch, heating the charcoal electrically, and condensing the released helium gas back into the helium vessel surrounding the sample space. The sample space contains up to four samples simultaneously and has four independent loading systems. On the top side of the gate valves, are four air locks that together with the sliding seal on the fluid path allows loading and unloading of samples without breaking the vacuum of the sample space. This improves throughput and reduces dramatically heat load to helium bath. By gradually inserting the sample, more than 95% of the sample heat is rejected to the cryocooler and only 30 J ends up in the bath for a 1 g sample. With this design a base temperature of less than 0.9 K can be sustained for more than three days. When the system is heavily used, the heat loads increases, but full day operation is achieved. The system is regenerated overnight to be ready for next day use.

The polarizer uses a closed fluid path to provide the sterile barrier. It is a sealed plastic component with all the pharmaceuticals pre-loaded. It can be single use and disposable for clinical use, but can be reused for non-sterile applications (*in vitro* and animal research). It has a vial that can hold up to 2 mL of sample. The vial is glued or welded to a long tube that allows it to reach the low temperature region. The other end of the tube is connected to a syringe with the solvent that sits outside the cryostat in a heater. Inside this outer tube is an inner tube, which allows solvent to be ejected onto the sample during dissolution. The syringe allows the solvent to

be heated to a desired temperature and released at a controlled flow rate. The dissolved sample returns along the outer tubing, past the syringe, and into the receiver where all the quality control is performed. A sliding seal on the outer tubing allows the sample to be moved through the cryostat without breaking the vacuum. In contrast to other published dissolution systems, where the solvent vapor pressure is the drive pressure for the solvent, this design allows independent control of solvent temperature and flow rate, which is critical in ensuring an optimal dissolution and full preservation of polarization for more complicated samples [28]. The fluid path has the advantage that the all-plastic component does not leach any paramagnetic metals into the sample that can reduce T_1 of the hyperpolarized agent.

Quality control is essential for clinical use of hyperpolarization. dDNP does not involve any chemistry, but is a complex compounding process. In the case of pyruvate, the most used formulation is based on pyruvic acid with trityl, and it involves a neutralization step. The pyruvic acid formulation is advantageous since neat pyruvic acid is 14 M, and a human dose can be achieved with approx. 1.5 g of pyruvic acid (or 1.2 mL). Other formulations with lower molarity require correspondingly larger sample volume. This is a requirement that needs to be considered for any agent formulation that will be translated to the clinic. In the case of pyruvate, the quality control involves measurement of pH, temperature, volume, pyruvate concentration, radical concentration (to verify removal) and polarization. These measurements are performed optically and by NMR without product contact. The time from start of dissolution to completion of all QC measurements is approx. 30 s. Even with 30 s, plus the time to inject, significant polarization is lost for agents with relatively short T_1 (e.g. glucose with a T_1 of ca 15 s). Hyperpolarization in general, pushes the boundaries of “bed side” pharmacy, and safety needs to be demonstrated by validation or quality control. For small animal studies, automated transfer and injection of the

hyperpolarized agent has been demonstrated, with a total time from dissolution to injection of approx. 5 s [29]. It is unlikely that this will be acceptable clinically, but it may be possible to reduce the time for QC, transfer and injection.

It has recently been shown that higher nuclear polarization can be obtained for both nitroxides and trityls by increasing the magnetic field strength [30–32] or lowering the temperature [27]. For [1-^{13}C]pyruvic acid, the ^{13}C polarization improved from 27% at 3.35 T to 60% at 4.64 T in the solid state and 60% at 7 T, all at 1-1.2 K.

Cross-polarization from protons to low gamma nuclei has proven to be very efficient for dilute proton systems and small samples [33]. At 6.7 T and 1.2 K a ^{13}C polarization of 78% with a time constant of 470 s was achieved for [^{13}C]urea. However, efficient cross-polarization has yet to be demonstrated for large samples with abundant protons. This is due to the strong dipolar broadening of the proton resonance (line width of 60-80 kHz) in fully protonated samples and the size of the sample, as well as the tendency of probe arcing in the helium atmosphere of the polarizer.

A centralized production site (within a city or region) for hyperpolarized solid samples could be imagined. Two approaches have been proposed [19,22]. In both cases long relaxation times (16-20 hours) have been demonstrated in a permanent magnetic field at liquid helium temperature. This could open up for during-the-day delivery of hyperpolarized solid samples, leaving only the dissolution and quality control at the local site. This is obviously, not only interesting for medical applications, but could open up for wider access to hyperpolarization.

Imaging

Hardware requirements

The sensitivity of the MR experiment is proportional to the polarization, which is created by the polarizer. For an MR scanner operating at a few megahertz or higher, the dominating source of noise is the imaged object (i.e. the patient), which scales linearly with frequency in the same way as the induced signal voltage. This means that a scanner field strength of only approx. 0.5 T should be sufficient to reach the crossover point between electronic and sample noise. However, for small coil elements (surface coils or array coils), or small animals, the required field strength is higher, and even at 3 T (32 MHz), it can be challenging to provide sufficient loading of the coil(s).

Standard clinical MR systems and coils are designed to transmit and receive radio frequency (RF) signals at ^{1}H resonance frequency only. However, multi-nuclear spectroscopy are available from most manufactures of whole body MR scanners. This option allows the system to perform MR experiments on non-proton nuclei of interest such as ^{13}C and ^{15}N. Multi-nuclear spectroscopy requires a broadband RF power amplifier, in addition to the standard ^{1}H narrowband amplifier. Secondly, the system will not have a built-in coil for transmission at the ^{13}C frequency. The ^{13}C coil can be designed for both transmission and reception, e.g. as a birdcage volume coil or surface coil, or reception can be by single or multiple coil elements in close proximity to the object. Narrowband low-noise-preamplifiers for ^{13}C are required that are built into the MR scanner or into the coil, with one preamplifier generally required for each receive channel. Since it is desirable to perform both ^{1}H anatomical imaging and hyperpolarized ^{13}C metabolic imaging during the same exam without repositioning the subject, the ^{13}C RF coil design and setup need to preserve the ability to perform ^{1}H imaging with minimal compromise of image quality. The coil configuration and design can be further optimized for imaging a

particular organ/anatomy. For example, in the first proof-of-concept clinical trial of hyperpolarized ^{13}C metabolic imaging in prostate cancer patients, a ^{13}C transmit-only volume coil built into a custom patient table was used in conjunction with a receive only endo-rectal coil containing both a ^{13}C and a ^{1}H element for signal reception. The scanner body coil was used for ^{1}H RF transmission during ^{1}H imaging [2]. A multi-channel ^{13}C receive-only array coil suited for other human applications, has also been demonstrated recently [34]. Receive-array coils may be particularly advantageous for hyperpolarized imaging in order to improve the encoding efficiency to cover the spatial, spectral and kinetic dimensions within the time window of the hyperpolarized signal. The challenge is however, to eliminate electronic noise for small coil elements at the relatively low ^{13}C resonance frequency (approx. 32 MHz). Regardless of the coil design and combination, the MR system needs to be configured such that the correct coils/channels are active or disabled during specific periods of the scans to avoid signal degradation due to coupling between coils.

Spatial encoding of the MR signal in imaging takes place by time-varying magnetic field gradients. It is important to note that for a given magnetic field gradient, the spatial variation in resonance frequency is proportional to the gyromagnetic ratio, and, thus, the maximum spatial resolution achievable for ^{13}C imaging is approximately a quarter of that of the proton under the same imaging conditions. Pulse sequences for ^{13}C imaging need to take this limitation into consideration.

It may be possible to circumvent the low gyromagnetic ratio limitation by transferring the ^{13}C or ^{15}N magnetization to neighboring ^{1}H nuclei for detection, see indirect detection further down. However, simultaneous RF transmission at both ^{1}H and the low γ nucleus frequencies is required for the polarization transfer pulse sequence, and this capability may not be available on

some clinical MR scanners. Proton decoupling during ^{13}C acquisition may be advantageous to remove long range couplings and increase T_2* [35].

Magnetic Resonance Spectroscopic Imaging (MRSI)

Hyperpolarized ^{13}C MR imaging requires acquisition of both the spatial distribution and kinetics of the metabolite signals. Early work in hyperpolarized ^{13}C imaging employed concentric phase encoding and variable flip angle [36] to acquire chemical shift images (CSI) in two dimensions within a time window that coincides with the maximum signal of metabolic products. The optimum acquisition depends on the bolus injection, the organ of interest, and perfusion. Typical CSI scan parameters would be a 16×16 matrix and 80 ms repetition time, i.e. a total scan time of 20 s. More efficient encoding can be achieved with Echo Planar Spectroscopic Imaging (EPSI). EPSI with flyback or symmetric gradient waveform traverses time and one spatial frequency domain in a single readout period, shortening the acquisition and allowing either single-time-point 3D MRSI or time-resolved multi-slice 2D MRSI (34,45) on a standard clinical 3T system (with a maximum gradient strength of 40 mT/m and slew rate of 150 mT/m/ms). There is a trade-off between spectral bandwidth and spatial resolution in the design of these gradient trajectories. Typically, a 5 mm resolution is achievable with 500 Hz spectral bandwidth without spectral aliasing of [1-^{13}C]pyruvate and its metabolic products (except ^{13}C-bicarbonate, which can be folded into a spectral region with no signal). On a pre-clinical MR scanner, 3D EPSI with high temporal resolution (2 s) has been demonstrated due to the better RF and gradient performance of the system [37]. A similar trade-off also exists for spiralCSI, which employs spiral readout gradients to sample a full plane in a single readout, and concatenates the spiral gradients multiple times for chemical shift encoding. However, even with multiple interleaves to minimize the impact of gradient slew-rate, the 2D spiral readout time can result in

a spectral bandwidth that is insufficient to fully cover the metabolite chemical shift range. On a clinical system, spiralCSI completes a 2D MRSI of a single slice in 375 ms, a 50-fold reduction in scan time compared to the conventional CSI method. However, for clinical applications that require a large FOV, spiralCSI acquisition time may increase drastically due to the increase of interleaves required to maintain the same spatial resolution and spectral bandwidth. In addition, spiralCSI encodes a circular FOV and can become inefficient for a region of interest with an asymmetric FOV. On the other hand, EPSI allows asymmetric FOV and the FOV in the one direction encoded by the EPSI readout is virtually unlimited due to the high sampling rate available on all clinical systems. The efficiency of the various acquisition schemes has been analyzed by Durst et al. [38].

Dynamic metabolic imaging can be used to determine rate constants, and signal averaging over the time course for each voxel can regain most of the SNR observed in optimized single time point methods. In pre-clinical studies, five dimensional (three spatial, the spectral and the kinetics), MRSI has been demonstrated by using spiralCSI and compressed sensing, both giving high quality images and dynamic curves. Taking advantage of the considerable sparsity in hyperpolarized ^{13}C spectra, compressed sensing pseudo-randomly under-sampled the spectral and two spatial dimensions during EPSI flyback readout, yields up to a factor of 7.53 in acceleration [39] relative to the conventional 3D EPSI sequence [40]. The acceleration can be used to improve spatial resolution and decrease acquisition time, or to cover a larger FOV, which will be useful for clinical applications. The tradeoff of this technique is the loss of metabolite peaks with low SNR.

Another approach is IDEAL spiralCSI [41]. IDEAL requires *a priori* information of the resonance frequencies of the ^{13}C metabolites to minimize the number of excitations for spectral

decoding. Spectral decoding is accomplished by varying the echo time (delay between excitation pulse and spiral magnetic field gradient) from excitation to excitation in an optimal way based on the number and specific spectral frequencies of the metabolites. There is no trade-off between spatial resolution and spectral bandwidth and therefore, the spatial resolution can be as high as SNR permits. This technique has been demonstrated in time-resolved 2D imaging, with a potential of combining with a pulse-and-acquire FID acquisition to obtain a spectrum to define the *a priori* information.

RF designs to optimize SNR

The signal from the injected, relatively concentrated, hyperpolarized ^{13}C substrate is initially often 5 to 10 times larger than the signals of its metabolic products. Multiband spectral-spatial RF excitation pulses [42] use spectral selectivity to excite the injected hyperpolarized ^{13}C substrate with a lower flip angle than the metabolic products. This way substrate polarization is preserved and product SNR maximized. The metabolic products are observable for a longer time than a uniformly constant flip angle strategy. A recent development combining multiband RF pulse design and compressed sensing random sampling created a sequence for time-resolved 3D MRSI acquisition [39,43] with good SNR. The flip-angle of the injected ^{13}C substrate and that of the products can be optimized for optimal CNR ratio for a particular organ or for disease characterization. An alternative to spectroscopically resolving multiple metabolites is to excite each metabolite selectively by a spectral-spatial pulse [40]. A multi-slice cardiac-gated sequence consisting of a large flip-angle spectral-spatial excitation pulse with a single-shot spiral trajectory was developed for ^{13}C imaging of cardiac metabolism [44]. The sequence alternates between the frequencies corresponding to each metabolite. Likewise, Gordon et al. [45] demonstrated a symmetric EPI with spectral-spatial excitation based on the product sequence available on a

clinical 3T scanner.The limitation of (spectral) selective excitation is that the length of the RF pulse often becomes long and leads to large signal loss during the pulse.

T_2-based sequences

Long T_2 relaxation times of ^{13}C metabolites were reported in a rat hepatocellular carcinoma (HCC) study [46] using a single-voxel preparation pulse followed by a train of spin-echoes to measure the T_2 decay of the signal within the voxel. T_2's of [1-^{13}C]alanine and [1-^{13}C]lactate were found to be longer in HCC tumors (1.2 s and 0.9 s, respectively) than in normal liver (0.4 s and 0.5 s, respectively). A large SNR gain is expected by using T_2-based sequences as compared to T_2*-based sequences. Most of the sequences discussed earlier are limited by signal decay given by T_2* that can be as long as 100 - 200 ms for [1-^{13}C]pyruvate, but is reduced to about 25 ms for [1-^{13}C]lactate and [1-^{13}C]alanine due to stronger J_{CH} coupling. T_2-based sequences, such as multi-echo balanced-Steady-State-Free-Precession (bSSFP) [47,48] and Fast Spin Echo EPSI (FSE-EPSI) [49], have significant signal gain and are excellent for single-time-point and dynamic MRSI. The challenge to utilize this strategy for time-resolved MRSI lies in the strong RF depletion during the echo train. In multi-echo bSSFP a series of gradient echoes are acquired between each RF pulse. The gradient echoes are used to spectrally decode the involved metabolites. More recently, the spectral selectivity of the RF pulse was exploited in a 3D bSSFP sequence to separate the spectral components of pyruvate and its metabolites as well as co-polarized urea [50]. The sequence was able to acquire a 32x16x16 spatial matrix in less than a second.

The long-range coupling from the C-1 carbon of lactate to the methyl protons, enables indirect detection of the carbon signal. Wang et al. [51] have recently demonstrated this in vivo on a clinical 3 T scanner in a murine tumor model using a reverse INEPT sequence. However, at

this point it is still unclear whether the theoretical sensitivity gain can be realized given the relaxation losses during transfer and the imperfections of pulses.

Kinetic modeling

Hyperpolarized pyruvate-to-lactate signal-time curves have been described by a two-site exchange [52] model. The conversion of [1-^{13}C]pyruvate to [1-^{13}C]lactate, as observed in hyperpolarized metabolic imaging, is a combination of flux (net creation of lactate) and exchange (^{13}C enrichment of the endogenous lactate pool). The impact of lactate pool size and proof of exchange was shown in cells preconditioned with unlabeled lactate. With increasing lactate pool size, an increase in the hyperpolarized [1-^{13}C]lactate was observed. The importance of exchange has been demonstrated in a lymphoma model by magnetization transfer between pyruvate and lactate after inversion of the magnetization for one of the species [53]. The authors concluded that the steady-state lactate pool size is likely the limiting factor of the observed hyperpolarized [1-^{13}C]lactate signal.

The availability of the reduced form of nicotimamide adenine dinucleotide, NADH, from sources beyond lactate dehydrogenase (LDH) catalyzed exchange, also impacts the conversion of hyperpolarized [1-^{13}C]pyruvate to [1-^{13}C]lactate. For example, added NADH from aldolase processing of ethanol in liver [54] has been shown to increase the flux of hyperpolarized [1-^{13}C]pyruvate to [1-^{13}C]lactate.

Under saturating conditions, the apparent rate constant, k_{pl}, increases as the pyruvate dose decreases [55]. The small-tip angle, pulse-and-acquire dynamic curves are biased by the substrate dose, bolus shape, and accumulated in flow of [1-^{13}C]lactate. These factors can be

eliminated by using a saturation recovery method [47], resulting in dynamic curves that describe the instantaneous metabolic conversion at the local tissue level during the passage of hyperpolarized [1-^{13}C]pyruvate.

For quantification of hyperpolarized spectra, a commonly used software is jMRUI [56]. For the estimation of kinetic rate constants, mathematical modeling is typically performed [41,57] to analyze the signal-time curves. It is not always required, since it was shown that the ratio of observed metabolites scales linearly with the kinetic rate constants estimated using mathematical modeling approaches [58,59]. In specific cases, it is possible to derive a mathematical framework, which calculates the kinetic rate constants directly based on the ratio of observed metabolites, and their longitudinal relaxation time, obliterating the need for using complex mathematical modeling [41]. The slowly varying kinetics (sparsity) of the metabolism can be exploited to accelerate the dynamic acquisition with methods such as k-t-PCA and k-t-SPARSE [60], using Principal Component Analysis and compressed sensing, respectively.

Applications

Oncology

The first clinical study of hyperpolarized ^{13}C-pyruvate metabolic imaging of prostate cancer patients was a Phase 1/2a Ascending-Dose Study to Assess the Safety and Tolerability and Imaging Potential of Hyperpolarized Pyruvate (^{13}C) Injection in Subjects with Prostate Cancer [2]. In this 33 patient study the primary objective was to assess the safety of the hyperpolarized pyruvate (^{13}C) injection. The secondary objectives were to determine: 1) The kinetics of hyperpolarized pyruvate injection delivery and metabolism in the prostate, and 2) to

determine the signal-to-noise-ratio (SNR) for ^{13}C pyruvate metabolites in regions of cancer as a function of the dose of the hyperpolarized pyruvate (^{13}C) injection. The highest dose level was well tolerated, and excellent contrast-to-noise for [1-^{13}C]lactate was observed in the tumor. The dynamic spectroscopy showed rapid bolus arrival of the hyperpolarized [1-^{13}C]pyruvate to the prostate, within 30 s; no detectable lactate in the normal prostate, but a large lactate signal from the cancer. When knowing the pharmacokinetics, the imaging could be initiated at the optimal time point, to generate metabolic maps from an EPSI sequence. Fig 3 shows an example of a patient that had a known abnormality in the right gland on the T_2 proton image, but nothing noticeable on the left side. However, the lactate/pyruvate image showed bilateral disease, which was later confirmed by pathology.

Using hyperpolarized [1-^{13}C]pyruvate, Hu et al. [61] studied liver metabolism in fasted rats and found higher lactate to alanine signal ratios and lower alanine signal level in the fasted rats than in free-fed rats. The low alanine signal is most likely due to a reduction of alanine aminotransferase (ALT) activity in fasted rat liver during gluconeogenesis. Alanine is also a good biomarker for hepatocellular carcinoma (HCC) detection. Using hyperpolarized [1-^{13}C]pyruvate, Darpolor et al. [62] found elevated alanine and lactate levels, consistent with enzyme expression analysis on rat HCC tissue extract. Interestingly, ^{13}C MRSI showed high alanine signals specifically in HCC tumors whereas it showed high lactate signals in the HCC tumors and in blood vessels. Low ^{13}C-alanine signals in vessels may be due to the much slower transport of alanine than lactate from cells to blood. Therefore, within the time window of hyperpolarization, little alanine signal was observed in vessels and normal liver.

Hyperpolarized pyruvate studies in glioma rat models [63,64] have shown that the lactate signal correlate with response to treatment. The pyruvate uptake was higher in the tumor than in

the normal brain due to the disruption of the blood brain barrier (BBB) in gliomas. The first human brain tumor case reports demonstrate both baseline lactate and bicarbonate signal in the normal brain, and differentiation of the lactate signal within the tumor [4,65].

Day et al. [52] reported decreased flux between pyruvate and lactate in lymphoma tumors when treated with etoposide and interrogated with hyperpolarized [1-^{13}C]pyruvate. Etoposide induces apoptosis and loss of NADH due to activation of poly-ADP-ribose-polymerase (PARP). Loss of the co-enzyme NADH leads to reduced LDH activity. Another hyperpolarized ^{13}C substrate that has been studied in lymphoma is 2-keto-[1-^{13}C]isocaproate (KIC) [66]. KIC is metabolized to leucine by branched chain amino acid transferase (BCAT), a biomarker for metastasis in some tumors and a target of proto-oncogene c-myc. Following injection of hyperpolarized KIC a 7-fold higher signal of ^{13}C-leucine in murine lymphoma than in healthy tissue was found. In the same study, no ^{13}C-leucine was observed in rat mammary adenocarcinoma. *Ex vivo* BCAT expression analysis yielded a high BCAT level in murine lymphoma and very low in rat mammary tumor, consistent with the hyperpolarized ^{13}C metabolic imaging findings. In a study of treatment response in lymphoma tumors with hyperpolarized [1,4-$^{13}C_2$]fumarate, Gallagher et al. [67] found that [1,4-$^{13}C_2$]malate from the labeled fumarate is a sensitive marker of necrosis. Fumarate uptake is slow, and malate is only observed in tissue with disintegrating cell membrane allowing fumarase to leak into the interstitial space. The conversion was 2.4-fold higher in etoposide-treated lymphoma tumors, and the malate signal correlated strongly with necrosis.

Cardiology

Generation and utilization of adenosine triphosphate, ATP, in the heart are tightly regulated by physiological conditions and energetic needs. The heart uses fatty acids,

carbohydrates and ketones as the substrates for energy production depending on availability. Altered myocardial substrate utilization is associated with diseases such as cardiomyopathy, hypertension, and diabetes; it also occurs during ischemia and reperfusion. Since all substrates are converted to acetyl-CoA prior to entering the Krebs cycle, measurement of the metabolic fluxes of acetyl-CoA production from various substrates can be used to monitor the changes in substrate selection and utilization. Pyruvate dehydrogenase (PDH) is the enzyme that decarboxylates the carbohydrate derived pyruvate to acetyl-CoA and CO_2, and the control of this enzyme's expression and activity is closely tied to myocardial substrate selection, thus the ability of using hyperpolarized ^{13}C pyruvate to non-invasively probe PDH flux is potentially a powerful diagnostic tool in cardiology.

Indeed, a number of recent reports in small and large animal models have demonstrated the ability of hyperpolarized ^{13}C MR imaging and spectroscopy to characterize the PDH flux non-invasively in normal hearts, and hearts during ischemia-reperfusion and cardiac disease [68–70]. In normal hearts, the $^{13}CO_2$ derived from [1-^{13}C]pyruvate due to cardiac PDH flux is observed mostly as ^{13}C-bicarbonate (in equilibrium with $^{13}CO_2$) signal in MR spectroscopy data, and some [1-^{13}C]lactate and [1-^{13}C]alanine signals can also be observed. In spatially resolved ^{13}C MR imaging data obtained from large animal models and human subjects, the substrate signal was found to be localized mostly in the cardiac chambers while ^{13}C-bicarbonate was localized in the myocardium; [1-^{13}C]lactate signal was more diffuse and observed in both the blood and cardiac muscle [3,71,72]. Recently, it was demonstrated that lactate produced in other organs, the liver predominantly, can bias estimation of the metabolism [73].

In models of ischemia and reperfusion, impaired PDH flux can be observed as decreased ^{13}C-bicarbonate signal shortly following reperfusion [68,74]. Potentially, the viability of the

affected tissue may be probed by following the recovery of the PDH flux (or the lack of it) post reperfusion and assessment of interventions targeting this metabolic pathway may also benefit from this technique. Change in PDH flux due to diabetes has been investigated in small animal models [70]. It has also been reported in a porcine pacing model of dilated cardiomyopathy (DCM) that disease progression can be followed non-invasively with ^{13}C metabolic imaging using hyperpolarized [1-^{13}C]pyruvate. Altered cardiac PDH flux was found to be strongly associated with onset of decompensated DCM [72]. Monitoring cardiac substrate utilization in patients may provide valuable information regarding progression of these diseases and aid clinical management.

Monitoring of cardiac Krebs cycle flux in real time using hyperpolarized [2-^{13}C]pyruvate is also feasible since the C2 position on pyruvate is carried into the cycle through acetyl-CoA (instead of being released as $^{13}CO_2$), and changes of Krebs cycle flux can be assessed by measuring changes in the [5-^{13}C]glutamate signal [75]. Along with PDH flux, these additional parameters obtainable by hyperpolarized ^{13}C MR provide insights into cardiac energetics and cellular environment that were not previously accessible non-invasively by other imaging modalities and may become valuable clinical tools in cardiology.

Although most of the efforts so far in utilizing hyperpolarized ^{13}C MR metabolic imaging in cardiology have been focused on probing substrate utilization using [1-^{13}C]pyruvate, ketone body utilization was recently studied in the rat heart [76]. The authors show that downstream metabolites (acetyl-carnitine and Krebs cycle intermediates) can be detected from both β-hydroxybutyrate and acetoacetate.

Neurology

Measuring blood brain barrier (BBB) transport, inflammation and redox in the brain, has the potential to address unmet clinical needs in neurodegenerative disease, traumatic brain injury and stroke. A substantial amount of pyruvate passes the normal BBB, and is converted into lactate and bicarbonate in brain tissue [77–79]. Thus, it should be possible to measure quantitatively BBB transport abnormalities and metabolism. However, a strategy to overcome the BBB transport limitation, explored the use of the more lipophilic ethyl ester of pyruvate [80].

Traumatic brain injury (TBI) is known to cause perturbations in the energy metabolism of the brain. The ^{13}C-bicarbonate signal was found to be 25% lower in the injured hemisphere compared with the non-injured hemisphere, while the hyperpolarized bicarbonate-to-lactate ratio was 34% lower in the injured hemisphere in rats with moderate TBI after injection of hyperpolarized [1-^{13}C]pyruvate [81].

Ethylpyruvate passes the BBB more efficiently than pyruvate due to the lipophilicity of the compound, and it hydrolyzes quickly to pyruvate and ethanol [80]. Ethylpyruvate has also been used therapeutically, and it may become a preferred substrate clinically for brain applications in the future. Several other dDNP agents have also been studied in the brain including ketoisocaproate (KIC) [82] and glucose [83]. KIC has higher uptake than pyruvate, and the leucine reported on branched-chain-amino-acid activity. With [2,3,4,6,6-$^{2}H_5$, 3,4-$^{13}C_2$]-D-glucose, the C-1 lactate signal was detected from the whole brain. All studies to date have been on the normal brain in rodents, and more studies in disease models will be required. Secondly, it is likely that clinical studies with pyruvate in patients with neurological disease will appear in the coming years. Some indication of the prospects for brain imaging is found in the initial brain tumor studies in patients (see oncology).

pH mapping

Many pathologies are associated with changes in tissue acid-base balance, including inflammation and ischemia [84,85]. For instance, most tumors have an acidic extracellular pH compared to normal tissue, and this can be correlated with prognosis and response to treatment [86,87]. Many chemotherapeutics are believed to be ineffective due to the acidic extracellular environment in tumors. Despite the importance of pH and its relationship to disease, there is currently no clinical tool available to image the spatial distribution of pH in humans. Gallagher et al have shown that hyperpolarized ^{13}C-bicarbonate can be used to map pH in tumors [88] by using the Henderson-Hasselbalch equation and the relative signals of ^{13}C-bicarbonate and $^{13}CO_2$. The tumor showed lower pH than the surrounding healthy tissues. Bicarbonate is a well-tolerated and has been used clinically already. However, it has two limitations: 1) the T_1 is relatively short in vivo, and 2) a significant fraction of the CO_2 exchanges on first pass in the lungs. Therefore, exogenous pH probes have been developed to overcome these limitations. Zymonic acid [89] and carbonates of glycerol [90] have longer T_1, and they have two intramolecular ^{13}C, one of which shifts with pH. It is also possible to determine pH from the CO_2 and bicarbonate produced when [1-^{13}C]pyruvate enters the Krebs cycle. In the heart, pH may also be assessed from the $^{13}CO_2$ and ^{13}C-bicarbonate produced from [1-^{13}C]pyruvate [69,75,91], if sufficient SNR is obtained for the $^{13}CO_2$ signal.

Redox imaging

An interesting imaging agent for the study of neurodegenerative disease may be [1-^{13}C]dehydroascorbic acid (DHA) [92,93]. This molecule is transported across the BBB by the GLUT1 transporter, and the conversion rate of DHA to ascorbate is a biomarker for oxidative stress. Von Morze et al investigated the ketone body ^{13}C-acetoacetate and its conversion to ^{13}C-β-hydroxybutyrate *in vivo*, catalyzed by β-hydroxybutyrate dehydrogenase as a marker of

mitochondrial redox state in the kidney of rats treated with metformin [94] (notice that the same substrate is also discussed under cardiology). Likewise, both the lactate-to-pyruvate [95] and the alanine-to-pyruvate [96] ratio is a biomarker of redox state being proportional to free cytosolic [NADH]/[NAD^+].

Outlook

dDNP is a research field in the infancy and the science is flourishing. This review presents state-of-the-art in field, as well as outlines some of the areas where further progress is needed to translate the technology to the clinic.

For hyperpolarized Metabolic MR to have a role in medical imaging relies on finding indications with a real unmet medical need. With currently more than twenty SPINlab installed worldwide and seven sites with approval for human use, the coming years open up for multi-site clinical trials and more extensive clinical research. At www.clinicaltrials.gov fifteen recruiting clinical studies can be found, involving hyperpolarized pyruvate. The outlook for hyperpolarized metabolic imaging is still very promising. The coming years will hopefully allow multi-site clinical trials to identify the patient populations that could form basis for full clinical development of hyperpolarized [1-^{13}C]pyruvate.

Acknowledgment

The author gratefully acknowledges the Danish National Research Foundation (DNRF124).

Biographical sketch

Jan H. Ardenkjaer-Larsen. b 1967. M.Sc.EE, 1991, Ph.D., 1995, Technical University of Denmark. Professor at the Department of Electrical Engineering, Technical University of Denmark and leader of the Center for Magnetic Resonance. For most of his career, he has been with pharmaceutical industry: Nycomed, Amersham, and GE Healthcare. Approx 150 papers and 28 patents in magnetic resonance and related aspects. Research interests: magnetic resonance imaging and hyperpolarization.

References

[1] J.H. Ardenkjaer-Larsen, B. Fridlund, A. Gram, G. Hansson, L. Hansson, M.H. Lerche, R. Servin, M. Thaning, K. Golman, Increase in signal-to-noise ratio of > 10,000 times in liquid-state NMR., Proc. Natl. Acad. Sci. U. S. A. 100 (2003) 10158–63. doi:10.1073/pnas.1733835100.

[2] S.J. Nelson, J. Kurhanewicz, D.B. Vigneron, P.E.Z. Larson, A.L. Harzstark, M. Ferrone, M. van Criekinge, J.W. Chang, R. Bok, I. Park, G. Reed, L. Carvajal, E.J. Small, P. Munster, V.K. Weinberg, J.H. Ardenkjaer-Larsen, A.P. Chen, R.E. Hurd, L.-I. Odegardstuen, F.J. Robb, J. Tropp, J.A. Murray, Metabolic Imaging of Patients with Prostate Cancer Using Hyperpolarized [1-13C]Pyruvate, Sci. Transl. Med. 5 (2013) 198ra108-198ra108. doi:10.1126/scitranslmed.3006070.

[3] C.H. Cunningham, J.Y. Lau, A.P. Chen, B.J. Geraghty, W.J. Perks, I. Roifman, G.A. Wright, K.A. Connelly, Hyperpolarized 13C Metabolic MRI of the Human Heart: Initial Experience., Circ. Res. (2016) CIRCRESAHA.116.309769-. doi:10.1161/CIRCRESAHA.116.309769.

[4] V.Z. Miloushev, K.L. Granlund, R. Boltyanskiy, S.K. Lyashchenko, L.M. DeAngelis, I.K. Mellinghoff, C.W. Brennan, V. Tabar, T.J. Yang, A.I. Holodny, R.E. Sosa, Y.W. Guo, A.P. Chen, J. Tropp, F. Robb, K.R. Keshari, Metabolic Imaging of the Human Brain with Hyperpolarized 13C Pyruvate Demonstrates 13C Lactate Production in Brain Tumor Patients., Cancer Res. (2018) canres.0221.2018. doi:10.1158/0008-5472.CAN-18-0221.

[5] R. Aggarwal, D.B. Vigneron, J. Kurhanewicz, Hyperpolarized 1-[13C]-Pyruvate Magnetic Resonance Imaging Detects an Early Metabolic Response to Androgen Ablation Therapy

in Prostate Cancer, Eur. Urol. 72 (2017) 1028–1029. doi:10.1016/J.EURURO.2017.07.022.

[6] B.M. Goodson, N. Whiting, A.M. Coffey, P. Nikolaou, F. Shi, B.M. Gust, M.E. Gemeinhardt, R. V. Shchepin, J.G. Skinner, J.R. Birchall, M.J. Barlow, E.Y. Chekmenev, Hyperpolarization Methods for MRS, in: EMagRes, John Wiley & Sons, Ltd, Chichester, UK, 2015: pp. 797–810. doi:10.1002/9780470034590.emrstm1457.

[7] A.W.A.W. Overhauser, Polarization of nuclei in metals, Phys. Rev. 92 (1953) 411. doi:10.1103/PhysRev.92.411.

[8] T.R. Carver, C.P. Slichter, Polarization of nuclear spins in metals, Phys. Rev. 92 (1953) 212.

[9] A. Abragam, W.G. Proctor, Experiments on Spin Temperature, Phys. Rev. 106 (1957) 160–161. doi:10.1103/PhysRev.106.160.

[10] C.D. Jeffries, Polarization of Nuclei by Resonance Saturation in Paramagnetic Crystals, Phys. Rev. 106 (1957) 164–165. doi:10.1103/PhysRev.106.164.

[11] A. Abragam, M. (Maurice) Goldman, Nuclear magnetism : order and disorder, Clarendon Press, 1982. http://findit.dtu.dk/en/catalog/2300286932 (accessed January 16, 2018).

[12] W.T. Wenckebach, Essentials of dynamic nuclear polarization, n.d. http://www.wenckebach.net/html/dnp-book.html (accessed February 5, 2018).

[13] W.T. Wenckebach, Spectral diffusion and dynamic nuclear polarization: Beyond the high temperature approximation, J. Magn. Reson. 284 (2017) 104–114. doi:10.1016/J.JMR.2017.10.001.

[14] W.T. Wenckebach, Dynamic nuclear polarization via thermal mixing: Beyond the high temperature approximation, J. Magn. Reson. 277 (2017) 68–78. doi:10.1016/J.JMR.2017.01.020.

[15] C.P. Slichter, Principles of Magnetic Resonance, Springer Berlin Heidelberg, Berlin, Heidelberg, 1990. doi:10.1007/978-3-662-09441-9.

[16] K.-N. Hu, Polarizing agents and mechanisms for high-field dynamic nuclear polarization of frozen dielectric solids, Solid State Nucl. Magn. Reson. 40 (2011) 31–41. doi:10.1016/j.ssnmr.2011.08.001.

[17] A.S. Lilly Thankamony, J.J. Wittmann, M. Kaushik, B. Corzilius, Dynamic nuclear polarization for sensitivity enhancement in modern solid-state NMR, Prog. Nucl. Magn. Reson. Spectrosc. 102–103 (2017) 120–195. doi:10.1016/j.pnmrs.2017.06.002.

[18] J.H. Ardenkjaer-Larsen, S. MacHoll, H. Jóhannesson, Dynamic Nuclear Polarization with Trityls at 1.2 K, Appl. Magn. Reson. 34 (2008) 509–522. doi:10.1007/s00723-008-0134-4.

[19] A. Capozzi, T. Cheng, G. Boero, C. Roussel, A. Comment, Thermal annihilation of photo-induced radicals following dynamic nuclear polarization to produce transportable frozen hyperpolarized 13C-substrates, Nat. Commun. 8 (2017) 15757. doi:10.1038/ncomms15757.

[20] K.R. Keshari, D.M. Wilson, Chemistry and biochemistry of 13C hyperpolarized magnetic resonance using dynamic nuclear polarization., Chem. Soc. Rev. 43 (2014) 1627–59. doi:10.1039/c3cs60124b.

[21] M. Karlsson, P.R. Jensen, J.Ø. Duus, S. Meier, M.H. Lerche, Development of Dissolution

DNP-MR Substrates for Metabolic Research, Appl. Magn. Reson. 43 (2012) 223–236. doi:10.1007/s00723-012-0336-7.

[22] X. Ji, A. Bornet, B. Vuichoud, J. Milani, D. Gajan, A.J. Rossini, L. Emsley, G. Bodenhausen, S. Jannin, Transportable hyperpolarized metabolites, Nat. Commun. 8 (2017) 13975. doi:10.1038/ncomms13975.

[23] S. Bowen, J.H. Ardenkjaer-Larsen, Formulation and utilization of choline based samples for dissolution dynamic nuclear polarization., J. Magn. Reson. 236 (2013) 26–30. doi:10.1016/j.jmr.2013.08.007.

[24] A. Comment, B. van den Brandt, K. Uffmann, F. Kurdzesau, S. Jannin, J.A. Konter, P. Hautle, W.T. Wenckebach, R. Gruetter, J.J. van der Klink, Principles of Operation of a DNP Prepolarizer Coupled to a Rodent MRI Scanner, Appl. Magn. Reson. 34 (2008) 313–319. doi:10.1007/s00723-008-0119-3.

[25] S. Bowen, J.H. Ardenkjaer-Larsen, Enhanced performance large volume dissolution-DNP, J. Magn. Reson. 240 (2014) 90–94. doi:10.1016/j.jmr.2014.01.009.

[26] B. Adeva, E. Arik, S. Ahmad, A. Arvidson, B. Badelek, M.K. Ballintijn, G. Bardin, G. Baum, P. Berglund, L. Betev, I.G. Bird, R. Birsa, P. Björkholm, B.E. Bonner, N. de Botton, M. Boutemeur, F. Bradamante, A. Bressan, A. Brüll, J. Buchanan, S. Bültmann, E. Burtin, C. Cavata, J.P. Chen, J. Clement, M. Clocchiatti, M.D. Corcoran, D. Crabb, J. Cranshaw, J. Çuhadar, S. Dalla Torre, A. Deshpande, R. van Dantzig, D. Day, S. Dhawan, C. Dulya, A. Dyring, S. Eichblatt, J.C. Faivre, D. Fasching, F. Feinstein, C. Fernandez, B. Frois, C. Garabatos, J.A. Garzon, T. Gaussiran, M. Giorgi, E. von Goeler, I.A. Golutvin, A. Gomez, G. Gracia, N. de Groot, M. Grosse Perdekamp, E. Gülmez, D. von Harrach, T.

Hasegawa, P. Hautle, N. Hayashi, C.A. Heusch, N. Horikawa, V.W. Hughes, G. Igo, S. Ishimoto, T. Iwata, M. de Jong, E.M. Kabuß, T. Kageya, R. Kaiser, A. Karev, H.J. Kessler, T.J. Ketel, I. Kiryushin, A. Kishi, Y. Kisselev, L. Klostermann, D. Krämer, V. Krivokhijine, V. Kukhtin, J. Kyynäräinen, M. Lamanna, U. Landgraf, K. Lau, T. Layda, J.M. Le Goff, F. Lehar, A. de Lesquen, J. Lichtenstadt, T. Lindqvist, M. Litmaath, S. Lopez-Ponte, M. Lowe, A. Magnon, G.K. Mallot, F. Marie, A. Martin, J. Martino, T. Matsuda, B. Mayes, J.S. McCarthy, K. Medved, G. van Middelkoop, D. Miller, J. Mitchell, K. Mori, J. Moromisato, G.S. Mutchler, A. Nagaitsev, J. Nassalski, L. Naumann, B. Neganov, T.O. Niinikoski, J.E.J. Oberski, A. Ogawa, S. Okumi, C.S. Özben, A. Penzo, C.A. Perez, F. Perrot-Kunne, D. Peshekhonov, R. Piegaia, L. Pinsky, S. Platchkov, M. Plo, D. Pose, H. Postma, J. Pretz, T. Pussieux, J. Pyrlik, I. Reyhancan, J.M. Rieubland, A. Rijllart, J.B. Roberts, S.E. Rock, M. Rodriguez, E. Rondio, O. Rondon, L. Ropelewski, A. Rosado, I. Sabo, J. Saborido, G. Salvato, A. Sandacz, D. Sanders, I. Savin, P. Schiavon, K.P. Schüler, R. Segel, R. Seitz, Y. Semertzidis, S. Sergeev, F. Sever, P. Shanahan, E. Sichtermann, G. Smirnov, A. Staude, A. Steinmetz, H. Stuhrmann, K.M. Teichert, F. Tessarotto, W. Thiel, M. Velasco, J. Vogt, R. Voss, R. Weinstein, C. Whitten, R. Willumeit, R. Windmolders, W. Wislicki, A. Witzmann, A. Yañez, N.I. Zamiatin, A.M. Zanetti, J. Zhao, Large enhancement of deuteron polarization with frequency modulated microwaves, Nucl. Instruments Methods Phys. Res. Sect. A Accel. Spectrometers, Detect. Assoc. Equip. 372 (1996) 339–343. doi:10.1016/0168-9002(95)01376-8.

[27] J.H. Ardenkjaer-Larsen, A.M. Leach, N. Clarke, J. Urbahn, D. Anderson, T.W. Skloss, Dynamic nuclear polarization polarizer for sterile use intent., NMR Biomed. 24 (2011) 927–32. doi:10.1002/nbm.1682.

[28] J. Jam, S. Dey, L. Muralidharan, A.M.A.M. Leach, J.H. Ardenkjaer-Larsen, Jet impingment melting with vaporization: A numerical study, in: 2008 Proc. ASME Summer Heat Transf. Conf. HT 2008, 2009: pp. 559–567. http://www.scopus.com/inward/record.url?eid=2-s2.0-70349120429&partnerID=tZOtx3y1.

[29] T. Cheng, M. Mishkovsky, J.A.M. Bastiaansen, O. Ouari, P. Hautle, P. Tordo, B. van den Brandt, A. Comment, Automated transfer and injection of hyperpolarized molecules with polarization measurement prior to in vivo NMR, NMR Biomed. 26 (2013) 1582–1588. doi:10.1002/nbm.2993.

[30] H. Jóhannesson, S. Macholl, J.H. Ardenkjaer-Larsen, Dynamic Nuclear Polarization of [1-13C]pyruvic acid at 4.6 tesla., J. Magn. Reson. 197 (2009) 167–175. doi:10.1016/j.jmr.2008.12.016.

[31] T. Cheng, A. Capozzi, Y. Takado, R. Balzan, A. Comment, Over 35% liquid-state 13C polarization obtained via dissolution dynamic nuclear polarization at 7 T and 1 K using ubiquitous nitroxyl radicals, Phys. Chem. Chem. Phys. 15 (2013) 20819–20822. doi:10.1039/C3CP53022A.

[32] H.A.I. Yoshihara, E. Can, M. Karlsson, M.H. Lerche, J. Schwitter, A. Comment, High-field dissolution dynamic nuclear polarization of [1- 13 C]pyruvic acid, Phys. Chem. Chem. Phys. 18 (2016) 12409–12413. doi:10.1039/C6CP00589F.

[33] A. Bornet, A. Pinon, A. Jhajharia, M. Baudin, X. Ji, L. Emsley, G. Bodenhausen, J.H. Ardenkjaer-Larsen, S. Jannin, Microwave-gated dynamic nuclear polarization, Phys. Chem. Chem. Phys. 18 (2016) 30530–30535. doi:10.1039/C6CP05587G.

[34] S. Ringgaard, R.F. Schulte, J. Tropp, C. Kögler, T. Lanz, M.A. Navarro, J.H. Ardenkjaer-Larsen, F. Robb, H. Stødkilde-Jørgensen, C. Laustsen, 13C RF coil combination for cardiac and abdominal human and pig studies, in: Proc. Intl. Soc. Mag. Reson. Med., 2016: p. 2152.

[35] A.P. Chen, J. Tropp, R.E. Hurd, M. Van Criekinge, L.G. Carvajal, D. Xu, J. Kurhanewicz, D.B. Vigneron, In vivo hyperpolarized 13C MR spectroscopic imaging with 1H decoupling., J. Magn. Reson. 197 (2009) 100–6. doi:10.1016/j.jmr.2008.12.004.

[36] K. Golman, R.I. Zandt, M. Lerche, R. Pehrson, J.H. Ardenkjaer-Larsen, R. in't Zandt, Metabolic imaging by hyperpolarized C-13 magnetic resonance imaging for in vivo tumor diagnosis, Cancer Res. 66 (2006) 10855–10860. doi:10.1158/0008-5472.CAN-06-2564.

[37] J. Wang, A.J. Wright, D. Hu, R. Hesketh, K.M. Brindle, Single shot three-dimensional pulse sequence for hyperpolarized ^{13} C MRI, Magn. Reson. Med. 77 (2017) 740–752. doi:10.1002/mrm.26168.

[38] M. Durst, U. Koellisch, A. Frank, G. Rancan, C. V. Gringeri, V. Karas, F. Wiesinger, M.I. Menzel, M. Schwaiger, A. Haase, R.F. Schulte, Comparison of acquisition schemes for hyperpolarised 13 C imaging, NMR Biomed. 28 (2015) 715–725. doi:10.1002/nbm.3301.

[39] P.E.Z. Larson, S. Hu, M. Lustig, A.B. Kerr, S.J. Nelson, J. Kurhanewicz, J.M. Pauly, D.B. Vigneron, Fast dynamic 3D MR spectroscopic imaging with compressed sensing and multiband excitation pulses for hyperpolarized 13C studies, Magn. Reson. Med. 65 (2011) 610–619. doi:10.1002/mrm.22650.

[40] C.H. Cunningham, A.P. Chen, M. Lustig, B. a Hargreaves, J. Lupo, D. Xu, J. Kurhanewicz, R.E. Hurd, J.M. Pauly, S.J. Nelson, D.B. Vigneron, Pulse sequence for

dynamic volumetric imaging of hyperpolarized metabolic products., J. Magn. Reson. 193 (2008) 139–46. doi:10.1016/j.jmr.2008.03.012.

[41] O. Khegai, R.F. Schulte, M.A. Janich, M.I. Menzel, E. Farrell, A.M. Otto, J.H. Ardenkjaer-Larsen, S.J. Glaser, A. Haase, M. Schwaiger, F. Wiesinger, Apparent rate constant mapping using hyperpolarized [1-(13)C]pyruvate., NMR Biomed. 27 (2014) 1256–65. doi:10.1002/nbm.3174.

[42] P.E.Z. Larson, A.B. Kerr, A.P. Chen, M.S. Lustig, M.L. Zierhut, S. Hu, C.H. Cunningham, J.M. Pauly, J. Kurhanewicz, D.B. Vigneron, Multiband excitation pulses for hyperpolarized 13C dynamic chemical-shift imaging., J. Magn. Reson. 194 (2008) 121–7. doi:10.1016/j.jmr.2008.06.010.

[43] P.E.Z. Larson, R. Bok, A.B. Kerr, M. Lustig, S. Hu, A.P. Chen, S.J. Nelson, J.M. Pauly, J. Kurhanewicz, D.B. Vigneron, Investigation of tumor hyperpolarized [1-13C]-pyruvate dynamics using time-resolved multiband RF excitation echo-planar MRSI., Magn. Reson. Med. 63 (2010) 582–91. doi:10.1002/mrm.22264.

[44] A.Z. Lau, A.P. Chen, N.R. Ghugre, V. Ramanan, W.W. Lam, K.A. Connelly, G.A. Wright, C.H. Cunningham, Rapid multislice imaging of hyperpolarized 13C pyruvate and bicarbonate in the heart, Magn. Reson. Med. 64 (2010) 1323–1331. doi:10.1002/mrm.22525.

[45] J.W. Gordon, D.B. Vigneron, P.E.Z. Larson, Development of a symmetric echo planar imaging framework for clinical translation of rapid dynamic hyperpolarized ^{13}C imaging, Magn. Reson. Med. 77 (2017) 826–832. doi:10.1002/mrm.26123.

[46] Y.-F. Yen, P. Le Roux, D. Mayer, R. King, D. Spielman, J. Tropp, K. Butts Pauly, A.

Pfefferbaum, S. Vasanawala, R. Hurd, T 2 relaxation times of 13 C metabolites in a rat hepatocellular carcinoma model measured in vivo using 13 C-MRS of hyperpolarized [1-13 C]pyruvate, NMR Biomed. 23 (2010) n/a-n/a. doi:10.1002/nbm.1481.

[47] J. Leupold, S. Månsson, J.S. Petersson, J. Hennig, O. Wieben, Fast multiecho balanced SSFP metabolite mapping of (1)H and hyperpolarized (13)C compounds., MAGMA. 22 (2009) 251–6. doi:10.1007/s10334-009-0169-z.

[48] J. Leupold, O. Wieben, S. Månsson, O. Speck, K. Scheffler, J.S. Petersson, J. Hennig, Fast chemical shift mapping with multiecho balanced SSFP, Magn. Reson. Mater. Physics, Biol. Med. 19 (2006) 267–273. doi:10.1007/s10334-006-0056-9.

[49] S. Månsson, J.S. Petersson, K. Scheffler, Fast metabolite mapping in the pig heart after injection of hyperpolarized 13C-pyruvate with low-flip angle balanced steady-state free precession imaging, Magn. Reson. Med. 68 (2012) 1894–1899. doi:10.1002/mrm.24183.

[50] H. Shang, S. Sukumar, C. von Morze, R.A. Bok, I. Marco-Rius, A. Kerr, G.D. Reed, E. Milshteyn, M.A. Ohliger, J. Kurhanewicz, P.E.Z. Larson, J.M. Pauly, D.B. Vigneron, Spectrally selective three-dimensional dynamic balanced steady-state free precession for hyperpolarized C-13 metabolic imaging with spectrally selective radiofrequency pulses, Magn. Reson. Med. 78 (2017) 963–975. doi:10.1002/mrm.26480.

[51] J. Wang, F. Kreis, A.J. Wright, R.L. Hesketh, M.H. Levitt, K.M. Brindle, Dynamic 1 H imaging of hyperpolarized [1- 13 C]lactate in vivo using a reverse INEPT experiment, Magn. Reson. Med. 79 (2018) 741–747. doi:10.1002/mrm.26725.

[52] S.E. Day, M.I. Kettunen, F.A. Gallagher, D.-E. Hu, M. Lerche, J. Wolber, K. Golman, J.H. Ardenkjaer-Larsen, K.M. Brindle, Detecting tumor response to treatment using

hyperpolarized 13C magnetic resonance imaging and spectroscopy, Nat. Med. 13 (2007) 1382–7. doi:10.1038/nm1650.

[53] M.I. Kettunen, D. Hu, T.H. Witney, R. McLaughlin, F. a Gallagher, S.E. Bohndiek, S.E. Day, K.M. Brindle, Magnetization transfer measurements of exchange between hyperpolarized [1-13C]pyruvate and [1-13C]lactate in a murine lymphoma., Magn. Reson. Med. 63 (2010) 872–80. doi:10.1002/mrm.22276.

[54] D.M. Spielman, D. Mayer, Y.-F. Yen, J. Tropp, R.E. Hurd, A. Pfefferbaum, In vivo measurement of ethanol metabolism in the rat liver using magnetic resonance spectroscopy of hyperpolarized [1-13C]pyruvate., Magn. Reson. Med. 62 (2009) 307–13. doi:10.1002/mrm.21998.

[55] M.L. Zierhut, Y.-F. Yen, A.P. Chen, R. Bok, M.J. Albers, V. Zhang, J. Tropp, I. Park, D.B. Vigneron, J. Kurhanewicz, R.E. Hurd, S.J. Nelson, Kinetic modeling of hyperpolarized 13C1-pyruvate metabolism in normal rats and TRAMP mice., J. Magn. Reson. 202 (2010) 85–92. doi:10.1016/j.jmr.2009.10.003.

[56] A. Naressi, C. Couturier, J.M. Devos, M. Janssen, C. Mangeat, R. de Beer, D. Graveron-Demilly, Java-based graphical user interface for the MRUI quantitation package, Magma Magn. Reson. Mater. Physics, Biol. Med. 12 (2001) 141–152. doi:10.1007/BF02668096.

[57] L. Menichetti, F. Frijia, A. Flori, F. Wiesinger, V. Lionetti, G. Giovannetti, G.D. Aquaro, F.A. Recchia, J.H. Ardenkjaer-Larsen, M.F. Santarelli, M. Lombardi, Assessment of real-time myocardial uptake and enzymatic conversion of hyperpolarized [1-^{13}C]pyruvate in pigs using slice selective magnetic resonance spectroscopy., Contrast Media Mol. Imaging. 7 (2012) 85–94. doi:10.1002/cmmi.480.

[58] D.K. Hill, Y. Jamin, M.R. Orton, N. Tardif, H.G. Parkes, S.P. Robinson, M.O. Leach, Y.-L. Chung, T.R. Eykyn, ^{1}H NMR and hyperpolarized ^{13}C NMR assays of pyruvate-lactate: a comparative study, NMR Biomed. 26 (2013) 1321–1325. doi:10.1002/nbm.2957.

[59] C.J. Daniels, M.A. McLean, R.F. Schulte, F.J. Robb, A.B. Gill, N. McGlashan, M.J. Graves, M. Schwaiger, D.J. Lomas, K.M. Brindle, F.A. Gallagher, A comparison of quantitative methods for clinical imaging with hyperpolarized ^{13}C-pyruvate, NMR Biomed. 29 (2016) 387–399. doi:10.1002/nbm.3468.

[60] P. Wespi, J. Steinhauser, G. Kwiatkowski, S. Kozerke, High-resolution hyperpolarized metabolic imaging of the rat heart using k - t PCA and k - t SPARSE, NMR Biomed. (2017) e3876. doi:10.1002/nbm.3876.

[61] S. Hu, A.P. Chen, M.L. Zierhut, R. Bok, Y.-F. Yen, M. a Schroeder, R.E. Hurd, S.J. Nelson, J. Kurhanewicz, D.B. Vigneron, In vivo carbon-13 dynamic MRS and MRSI of normal and fasted rat liver with hyperpolarized 13C-pyruvate., Mol. Imaging Biol. 11 (2009) 399–407. doi:10.1007/s11307-009-0218-z.

[62] M.M. Darpolor, Y.-F. Yen, M.-S. Chua, L. Xing, R.H. Clarke-Katzenberg, W. Shi, D. Mayer, S. Josan, R.E. Hurd, A. Pfefferbaum, L. Senadheera, S. So, L. V. Hofmann, G.M. Glazer, D.M. Spielman, In vivo MRSI of hyperpolarized [1-13C]pyruvate metabolism in rat hepatocellular carcinoma, NMR Biomed. 24 (2011) 506–513. doi:10.1002/nbm.1616.

[63] I. Park, R. Bok, T. Ozawa, J.J. Phillips, C.D. James, D.B. Vigneron, S.M. Ronen, S.J. Nelson, Detection of early response to temozolomide treatment in brain tumors using hyperpolarized 13C MR metabolic imaging, J. Magn. Reson. Imaging. 33 (2011) 1284–

1290. doi:10.1002/jmri.22563.

[64] S.E. Day, M.I. Kettunen, M.K. Cherukuri, J.B. Mitchell, M.J. Lizak, H.D. Morris, S. Matsumoto, A.P. Koretsky, K.M. Brindle, Detecting response of rat C6 glioma tumors to radiotherapy using hyperpolarized [1- 13C]pyruvate and 13C magnetic resonance spectroscopic imaging., Magn. Reson. Med. 65 (2011) 557–63. doi:10.1002/mrm.22698.

[65] I. Park, P.E.Z. Larson, J.W. Gordon, L. Carvajal, H.-Y. Chen, R. Bok, M. Van Criekinge, M. Ferrone, J.B. Slater, D. Xu, J. Kurhanewicz, D.B. Vigneron, S. Chang, S.J. Nelson, Development of methods and feasibility of using hyperpolarized carbon-13 imaging data for evaluating brain metabolism in patient studies, Magn. Reson. Med. 80 (2018) 864–873. doi:10.1002/mrm.27077.

[66] M. Karlsson, P.R. Jensen, R. in 't Zandt, A. Gisselsson, G. Hansson, J.Ø. Duus, S. Meier, M.H. Lerche, Imaging of branched chain amino acid metabolism in tumors with hyperpolarized 13C ketoisocaproate, Int. J. Cancer. 127 (2010) 729–736. doi:10.1002/ijc.25072.

[67] F.A. Gallagher, M.I. Kettunen, D.-E. Hu, P.R. Jensen, R. In 't Zandt, M. Karlsson, A. Gisselsson, S.K. Nelson, T.H. Witney, S.E. Bohndiek, G. Hansson, T. Peitersen, M.H. Lerche, K.M. Brindle, Production of hyperpolarized [1,4-13C2]malate from [1,4-13C2]fumarate is a marker of cell necrosis and treatment response in tumors., Proc. Natl. Acad. Sci. U. S. A. 106 (2009) 19801–6. doi:10.1073/pnas.0911447106.

[68] K. Golman, J.S. Petersson, P. Magnusson, E. Johansson, P. Akeson, C.-M. Chai, G. Hansson, S. Månsson, Cardiac metabolism measured noninvasively by hyperpolarized 13C MRI., Magn. Reson. Med. 59 (2008) 1005–13. doi:10.1002/mrm.21460.

[69] M.E. Merritt, C. Harrison, C. Storey, F.M. Jeffrey, a D. Sherry, C.R. Malloy, Hyperpolarized 13C allows a direct measure of flux through a single enzyme-catalyzed step by NMR., Proc. Natl. Acad. Sci. U. S. A. 104 (2007) 19773–7. doi:10.1073/pnas.0706235104.

[70] M. a Schroeder, L.E. Cochlin, L.C. Heather, K. Clarke, G.K. Radda, D.J. Tyler, In vivo assessment of pyruvate dehydrogenase flux in the heart using hyperpolarized carbon-13 magnetic resonance., Proc. Natl. Acad. Sci. U. S. A. 105 (2008) 12051–6. doi:10.1073/pnas.0805953105.

[71] F. Frijia, M.F. Santarelli, U. Koellisch, G. Giovannetti, T. Lanz, A. Flori, M. Durst, G.D. Aquaro, R.F. Schulte, D. De Marchi, V. Lionetti, J.H. Ardenkjaer-Larsen, L. Landini, L. Menichetti, V. Positano, 16-channel surface coil for^{13}C-hyperpolarized spectroscopic imaging of cardiac metabolism in pig heart, J. Med. Biol. Eng. 36 (2016). doi:10.1007/s40846-016-0113-4.

[72] M.A. Schroeder, A.Z. Lau, A.P. Chen, Y. Gu, J. Nagendran, J. Barry, X. Hu, J.R.B. Dyck, D.J. Tyler, K. Clarke, K.A. Connelly, G.A. Wright, C.H. Cunningham, Hyperpolarized 13 C magnetic resonance reveals early-and late-onset changes to in vivo pyruvate metabolism in the failing heart, Eur. J. Heart Fail. 15 (2013) 130–140. doi:10.1093/eurjhf/hfs192.

[73] P. Wespi, J. Steinhauser, G. Kwiatkowski, S. Kozerke, Overestimation of cardiac lactate production caused by liver metabolism of hyperpolarized [1- ^{13} C]pyruvate, Magn. Reson. Med. (2018). doi:10.1002/mrm.27197.

[74] M.E. Merritt, C. Harrison, C. Storey, A.D. Sherry, C.R. Malloy, Inhibition of carbohydrate oxidation during the first minute of reperfusion after brief ischemia: NMR

detection of hyperpolarized 13CO2 and H13CO 3−, Magn. Reson. Med. 60 (2008) 1029–1036. doi:10.1002/mrm.21760.

[75] A.P. Chen, R.E. Hurd, M.A. Schroeder, A.Z. Lau, Y. Gu, W.W. Lam, J. Barry, J. Tropp, C.H. Cunningham, Simultaneous investigation of cardiac pyruvate dehydrogenase flux, Krebs cycle metabolism and pH, using hyperpolarized [1,2-13C2]pyruvate in vivo, NMR Biomed. 25 (2012) 305–311. doi:10.1002/nbm.1749.

[76] J.J. Miller, D.R. Ball, A.Z. Lau, D.J. Tyler, Hyperpolarized ketone body metabolism in the rat heart, NMR Biomed. (2018) e3912. doi:10.1002/nbm.3912.

[77] D. Mayer, Y.-F. Yen, A. Takahashi, S. Josan, J. Tropp, B.K. Rutt, R.E. Hurd, D.M. Spielman, A. Pfefferbaum, Dynamic and high-resolution metabolic imaging of hyperpolarized [1-13C]-pyruvate in the rat brain using a high-performance gradient insert, Magn. Reson. Med. 65 (2011) 1228–1233. doi:10.1002/mrm.22707.

[78] M. Marjańska, I. Iltis, A.A. Shestov, D.K. Deelchand, C. Nelson, K. Uğurbil, P.-G. Henry, In vivo 13C spectroscopy in the rat brain using hyperpolarized [1-13C]pyruvate and [2-13C]pyruvate, J. Magn. Reson. 206 (2010) 210–218. doi:10.1016/j.jmr.2010.07.006.

[79] J.M. Park, S. Josan, T. Grafendorfer, Y.-F. Yen, R.E. Hurd, D.M. Spielman, D. Mayer, Measuring mitochondrial metabolism in rat brain in vivo using MR Spectroscopy of hyperpolarized [2-13C]pyruvate, NMR Biomed. 26 (2013) 1197–1203. doi:10.1002/nbm.2935.

[80] R.E. Hurd, Y.-F. Yen, D. Mayer, A. Chen, D. Wilson, S. Kohler, R. Bok, D. Vigneron, J. Kurhanewicz, J. Tropp, D. Spielman, A. Pfefferbaum, Metabolic imaging in the anesthetized rat brain using hyperpolarized [1-13C] pyruvate and [1-13C] ethyl pyruvate.,

Magn. Reson. Med. 63 (2010) 1137–43. doi:10.1002/mrm.22364.

[81] S.J. DeVience, X. Lu, J. Proctor, P. Rangghran, E.R. Melhem, R. Gullapalli, G.M. Fiskum, D. Mayer, Metabolic imaging of energy metabolism in traumatic brain injury using hyperpolarized [1-13C]pyruvate, Sci. Rep. 7 (2017) 1907. doi:10.1038/s41598-017-01736-x.

[82] S.A. Butt, L. V. Søgaard, P.O. Magnusson, M.H. Lauritzen, C. Laustsen, P. Åkeson, J.H. Ardenkjær-Larsen, P. Keson, J.H. Ardenkjær-Larsen, Imaging cerebral 2-ketoisocaproate metabolism with hyperpolarized 13C Magnetic Resonance Spectroscopic Imaging, J. Cereb. Blood Flow Metab. 32 (2012) 1508–1514. doi:10.1038/jcbfm.2012.34.

[83] M. Mishkovsky, B. Anderson, M. Karlsson, M.H. Lerche, A.D. Sherry, R. Gruetter, Z. Kovacs, A. Comment, Measuring glucose cerebral metabolism in the healthy mouse using hyperpolarized 13C magnetic resonance, Sci. Rep. 7 (2017) 11719. doi:10.1038/s41598-017-12086-z.

[84] H.J. Adrogué, F.J. Gennari, J.H. Galla, N.E. Madias, Assessing acid-base disorders., Kidney Int. 76 (2009) 1239–47. doi:10.1038/ki.2009.359.

[85] J.R. Casey, S. Grinstein, J. Orlowski, Sensors and regulators of intracellular pH., Nat. Rev. Mol. Cell Biol. 11 (2010) 50–61. doi:10.1038/nrm2820.

[86] N. Raghunand, X. He, R. van Sluis, B. Mahoney, B. Baggett, C.W. Taylor, G. Paine-Murrieta, D. Roe, Z.M. Bhujwalla, R.J. Gillies, Enhancement of chemotherapy by manipulation of tumour pH., Br. J. Cancer. 80 (1999) 1005–11. doi:10.1038/sj.bjc.6690455.

[87] I.F. Robey, B.K. Baggett, N.D. Kirkpatrick, D.J. Roe, J. Dosescu, B.F. Sloane, A.I. Hashim, D.L. Morse, N. Raghunand, R.A. Gatenby, R.J. Gillies, Bicarbonate increases tumor pH and inhibits spontaneous metastases., Cancer Res. 69 (2009) 2260–8. doi:10.1158/0008-5472.CAN-07-5575.

[88] F.A. Gallagher, M.I. Kettunen, S.E. Day, D.-E. Hu, J.H. Ardenkjaer-Larsen, R. in 't 't 't Zandt, P.R. Jensen, M. Karlsson, K. Golman, M.H. Lerche, K.M. Brindle, J.H. Ardenkjær-Larsen, R. in 't 't 't Zandt, P.R. Jensen, M. Karlsson, K. Golman, M.H. Lerche, K.M. Brindle, Magnetic resonance imaging of pH in vivo using hyperpolarized 13C-labelled bicarbonate, Nature. 453 (2008) 940–943. doi:10.1038/nature07017.

[89] S. Düwel, C. Hundshammer, M. Gersch, B. Feuerecker, K. Steiger, A. Buck, A. Walch, A. Haase, S.J. Glaser, M. Schwaiger, F. Schilling, Imaging of pH in vivo using hyperpolarized 13C-labelled zymonic acid, Nat. Commun. 8 (2017) 15126. doi:10.1038/ncomms15126.

[90] D.E. Korenchan, R.R. Flavell, C. Baligand, R. Sriram, K. Neumann, S. Sukumar, H. VanBrocklin, D.B. Vigneron, D.M. Wilson, J. Kurhanewicz, Dynamic nuclear polarization of biocompatible (13)C-enriched carbonates for in vivo pH imaging., Chem. Commun. (Camb). 52 (2016) 3030–3. doi:10.1039/c5cc09724j.

[91] A.Z. Lau, J.J. Miller, D.J. Tyler, Mapping of intracellular pH in the in vivo rodent heart using hyperpolarized [1-13C]pyruvate, Magn. Reson. Med. 77 (2017) 1810–1817. doi:10.1002/mrm.26260.

[92] S.E. Bohndiek, M.I. Kettunen, D. Hu, B.W.C. Kennedy, J. Boren, F.A. Gallagher, K.M. Brindle, Hyperpolarized [1- 13 C]-Ascorbic and Dehydroascorbic Acid: Vitamin C as a

Probe for Imaging Redox Status in Vivo, J. Am. Chem. Soc. 133 (2011) 11795–11801. doi:10.1021/ja2045925.

[93] K.R. Keshari, J. Kurhanewicz, R. Bok, P.E.Z. Larson, D.B. Vigneron, D.M. Wilson, Hyperpolarized 13C dehydroascorbate as an endogenous redox sensor for in vivo metabolic imaging., Proc. Natl. Acad. Sci. U. S. A. 108 (2011) 18606–11. doi:10.1073/pnas.1106920108.

[94] C. von Morze, M.A. Ohliger, I. Marco-Rius, D.M. Wilson, R.R. Flavell, D. Pearce, D.B. Vigneron, J. Kurhanewicz, Z.J. Wang, Direct assessment of renal mitochondrial redox state using hyperpolarized 13 C-acetoacetate, Magn. Reson. Med. (2018). doi:10.1002/mrm.27054.

[95] C.E. Christensen, M. Karlsson, J.R. Winther, R. Jensen, M.H. Lerche, Non-invasive In-cell Determination of Free Cytosolic [NAD ⁺]/ [NADH] Ratios Using Hyperpolarized Glucose Show Large Variations in Metabolic Phenotypes *, (2013). doi:10.1074/jbc.M113.498626.

[96] J.M. Park, C. Khemtong, S.-C. Liu, R.E. Hurd, D.M. Spielman, In vivo assessment of intracellular redox state in rat liver using hyperpolarized [1- ^{13} C]Alanine, Magn. Reson. Med. 77 (2017) 1741–1748. doi:10.1002/mrm.26662.

[97] A.P. Chen, J. Kurhanewicz, R. Bok, D. Xu, D. Joun, V. Zhang, S.J. Nelson, R.E. Hurd, D.B. Vigneron, Feasibility of using hyperpolarized [1-13C]lactate as a substrate for in vivo metabolic 13C MRSI studies., Magn. Reson. Imaging. 26 (2008) 721–6. doi:10.1016/j.mri.2008.01.002.

[98] I. Marco-Rius, P. Cao, C. von Morze, M. Merritt, K.X. Moreno, G.-Y. Chang, M.A.

Ohliger, D. Pearce, J. Kurhanewicz, P.E.Z. Larson, D.B. Vigneron, Multiband spectral-spatial RF excitation for hyperpolarized [2- ^{13} C]dihydroxyacetone ^{13} C-MR metabolism studies, Magn. Reson. Med. 77 (2017) 1419–1428. doi:10.1002/mrm.26226.

[99] K.R. Keshari, D.M. Wilson, A.P. Chen, R. Bok, P.E.Z. Larson, S. Hu, M. Van Criekinge, J.M. Macdonald, D.B. Vigneron, J. Kurhanewicz, Hyperpolarized [2-13C]-fructose: a hemiketal DNP substrate for in vivo metabolic imaging., J. Am. Chem. Soc. 131 (2009) 17591–6. doi:10.1021/ja9049355.

[100] C. Canapè, G. Catanzaro, E. Terreno, M. Karlsson, M.H. Lerche, P.R. Jensen, Probing treatment response of glutaminolytic prostate cancer cells to natural drugs with hyperpolarized [5- ^{13} C]glutamine, Magn. Reson. Med. 73 (2015) 2296–2305. doi:10.1002/mrm.25360.

[101] A. Flori, M. Liserani, F. Frijia, G. Giovannetti, V. Lionetti, V. Casieri, V. Positano, G.D. Aquaro, F.A. Recchia, M.F. Santarelli, L. Landini, J.H. Ardenkjaer-Larsen, L. Menichetti, Real-time cardiac metabolism assessed with hyperpolarized [1-(13) C]acetate in a large-animal model., Contrast Media Mol. Imaging. 10 (2014) 194–202. doi:10.1002/cmmi.1618.

[102] U. Koellisch, C. Laustsen, T.S. Nørlinger, J.A. Østergaard, A. Flyvbjerg, C. V. Gringeri, M.I. Menzel, R.F. Schulte, A. Haase, H. Stødkilde-Jørgensen, Investigation of metabolic changes in STZ-induced diabetic rats with hyperpolarized [1-13C]acetate, Physiol. Rep. 3 (2015) e12474. doi:10.14814/phy2.12474.

[103] C. von Morze, R.A. Bok, G.D. Reed, J.H. Ardenkjaer-Larsen, J. Kurhanewicz, D.B. Vigneron, Simultaneous multiagent hyperpolarized (13)C perfusion imaging., Magn.

Reson. Med. 72 (2014) 1599–609. doi:10.1002/mrm.25071.

[104] E.S.S. Hansen, N.J. Stewart, J.M. Wild, H. Stødkilde-Jørgensen, C. Laustsen, Hyperpolarized 13C,15N2-Urea MRI for assessment of the urea gradient in the porcine kidney, Magn. Reson. Med. (2016) n/a-n/a. doi:10.1002/mrm.26483.

[105] C. von Morze, R.A. Bok, G.D. Reed, J.H. Ardenkjaer-Larsen, J. Kurhanewicz, D.B. Vigneron, Simultaneous multiagent hyperpolarized 13C perfusion imaging, Magn. Reson. Med. (2013) n/a-n/a. doi:10.1002/mrm.25071.

[106] J.M. Park, M. Wu, K. Datta, S.-C. Liu, A. Castillo, H. Lough, D.M. Spielman, K.L. Billingsley, Hyperpolarized Sodium [1- 13 C]-Glycerate as a Probe for Assessing Glycolysis In Vivo, J. Am. Chem. Soc. 139 (2017) 6629–6634. doi:10.1021/jacs.7b00708.

[107] R.M. Malinowski, K.W. Lipsø, M.H. Lerche, J.H. Ardenkjær-Larsen, Dissolution Dynamic Nuclear Polarization capability study with fluid path, J. Magn. Reson. 272 (2016). doi:10.1016/j.jmr.2016.09.015.

Table 1. Imaging agents that have been polarized with dDNP and imaged in vivo

Agent	Products	REF
[1-^{13}C]pyruvate	[1-^{13}C]lactate, [1-^{13}C]alanine, [^{13}C] bicarbonate, $^{13}CO_2$	[36]
[2-^{13}C]pyruvate	[2-^{13}C]lactate, [2-^{13}C]alanine, [1-^{13}C]acetyl-carnitine, [1-^{13}C]citrate, [5-^{13}C]glutamate	[78]
[1,2-$^{13}C_2$]pyruvate	[1,2-$^{13}C_2$]lactate, [1,2-$^{13}C_2$]alanine, [1-^{13}C]acetyl-carnitine, [1-^{13}C]citrate, [5-^{13}C]glutamate, [^{13}C]bicarbonate, $^{13}CO_2$	[75]
[1-^{13}C]lactate	[1-^{13}C]pyruvate, [1-^{13}C]alanine, [^{13}C] bicarbonate, $^{13}CO_2$	[97]
^{13}C-bicarbonate	$^{13}CO_2$	[88]
[1,4-$^{13}C_2$]fumarate	[1,4-$^{13}C_2$]malate	[67]
[2-^{13}C]dihydroxyacetone	[2-^{13}C]glycerol-3-phosphate, [2-^{13}C]phosphoenolpyruvate	[98]
[2-^{13}C]fructose	[1-^{13}C]fructose-6-phosphate	[99]
[5-^{13}C]glutamine	[5-^{13}C]glutamate	[100]
[1-^{13}C]ethylpyruvate	[1-^{13}C]pyruvate, [1-^{13}C]lactate, [1-^{13}C]alanine, [^{13}C] bicarbonate, $^{13}CO_2$	[80]
[U-$^{13}C_2$,U-^{2}H]glucose	Full glycolysis, lactate, alanine, bicarbonate	[83]
[1-^{13}C]acetate	[1-^{13}C]acetylcarnitine	[101,102]
[^{13}C]urea/[^{13}C,$^{15}N_2$]urea	none	[103,104]
bis-1,1-(hydroxymethyl)-[1-^{13}C]cyclopropane-d8 (HP001)	none	[105]
α-keto-[1-^{13}C]isocaproate	[1-^{13}C]leucine	[82]
[1-^{13}C]dehydroascorbic acid	[1-^{13}C]ascorbic acid	[92,93]
[1-^{13}C]alanine	[1-^{13}C]lactate, [1-^{13}C]pyruvate, [^{13}C]bicarbonate	[96]
[1-^{13}C]glycerate	[1-^{13}C]pyruvate, [1-^{13}C]lactate	[106]
[1,3-$^{13}C_2$]acetoacetate	[1,3-$^{13}C_2$]β-hydroxybutyrate, [1-^{13}C]acetyl-carnitine, [5-^{13}C]glutamate, [1-^{13}C]citrate	[76,94]
[1-^{13}C]β-hydroxybutyrate	[1,3-$^{13}C_2$]acetoacetate, [1-^{13}C]acetyl-carnitine	[76]

Figure Captions

Fig. 1: The principle of dDNP is illustrated. At room temperature and 3 T the ^{13}C nuclear spins are only weakly polarized to about 2.5 ppm, left graph. However, electron spins have a 2,700 times stronger magnetic moment and are easily polarized. When the sample is cooled the electron spin polarization reaches almost unity (97.8% at 3.35 T and 1 K). By irradiation with microwaves close to the resonance frequency of the electron spins, electron-electron-nuclear transitions are induced, and the nuclear spin polarization will be enhanced hundred-fold by DNP to several tens of percent. This process is slow at low temperatures, and takes typically 15-60 min. When the sample is polarized, superheated water or buffer dissolves the sample within seconds, and a room temperature solution of the hyperpolarized molecule is obtained. The hyperpolarized nuclear spins relax to thermal equilibrium (e.g. 2.5 ppm) with the longitudinal realaxation constant, T_1, of typically 40-80 s for carboxylic acids. A hyperpolarized ^{13}C spectrum of urea obtained in a single transient is shown to the right along with the thermal spectrum after 65 h of averaging.

Fig 2: Different polarizer generations. The original polarizer design was described in [1]. This polarizer was installed in a clean room at UCSF for the patient study published in [2]. Oxford Instruments commercialized the Hypersense under license from General Electric. Later General Electric introduced the SPINlab for clinical studies [27].

Fig 3: (A) SPINlab polarizer. The polarizer operates at 5 T and 0.9 K. The polarizer has four independent channels that allow simultaneous polarization of up to four samples (fluid paths).

The QC module (cylindrical black unit) is seen to the right of the photo below the touch screen. (B) Fluid Path (FP). (1) vial, (2) dynamic seal, (3) co-axial tube, (4) valve, (5) dissolution syringe, (6) transfer tube, (7) EPA filter, (8) receiver vessel, (9) QC appendage, (10) sterile assurance filter (11), and Medrad 65 mL MR syringe. The vial loads into the polarizer (behind the sliding door). The vial is inserted into one of the four airlocks and the dissolution syringe is inserted into the corresponding heater-pressure module. After some pump-flush cycles, the airlock gate-valve will open and the vial can be pushed through the dynamic seal to the 0.9 K sample space. The receiver vessel is initially loaded into the corresponding warmer module seen to the lower right in (A). Shortly before dissolution the receiver vessel is moved from the warmer to the QC module. Reproduced with permission from [107]. © Elsevier.

Fig 4: 2D single–time point MRSI data. Images were obtained from a patient with serum PSA of 9.5 ng/mL, who was diagnosed with bilateral biopsy-proven Gleason grade 3 + 3 prostate cancer and received the highest dose of hyperpolarized [1-^{13}C]pyruvate (0.43 mL/kg). The axial T_2-weighted image shows a unilateral region of reduced signal intensity (red arrows), which is consistent with a reduction in the corresponding ADC. The ^{1}H spectral arrays supported these findings, with voxels with reduced citrate and elevated choline/citrate (highlighted in pink) on the right side of the gland and voxels with normal metabolite ratios on the left side. The ^{13}C spectral arrays show voxels with elevated levels of hyperpolarized [1-^{13}C]lactate/[1-^{13}C]pyruvate (highlighted in pink) on both the right and left sides of the prostate. The location of colored regions in the metabolite image overlay had a ratio of [1-^{13}C]lactate/[1-^{13}C]pyruvate greater than or equal to 0.6. Reproduced with permission from [2]. © Science.

Fig 5: Cardiac ^{13}C images from human subject displayed as color overlays on top of grayscale anatomical images. The [1-^{13}C]pyruvate substrate (a) is seen mainly in the blood pool within the cardiac chambers. Flux of pyruvate through the pyruvate dehydrogenase complex is reflected in the ^{13}C-bicarbonate image (b). The [1-^{13}C]lactate product (c) appeared with a diffuse distribution covering the muscle and chambers. Representative ^{13}C spectrum (d) of substrate and products from the heart of the subject. Adapted with permission from [3]. © American Heart Association.

FIG 1:

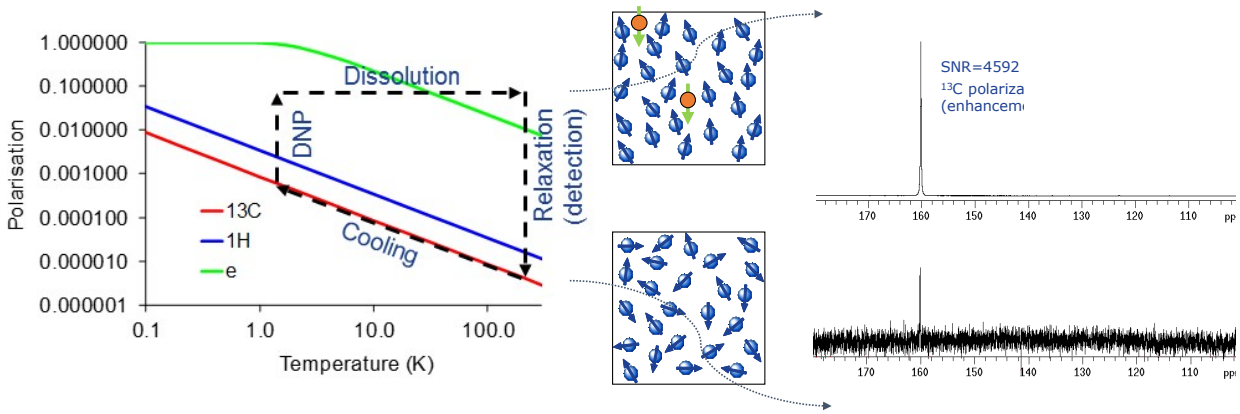
1.000000
0.100000
0.010000
0.001000
0.000100
0.000010
0.000001
Polarisation
0.1
1.0
10.0
100.0
Temperature (K)
Dissolution
DNP
Cooling
Relaxation
(detection)
13C
1H
e
SNR=4592
170
160
150
140
130
120
110

FIG 2

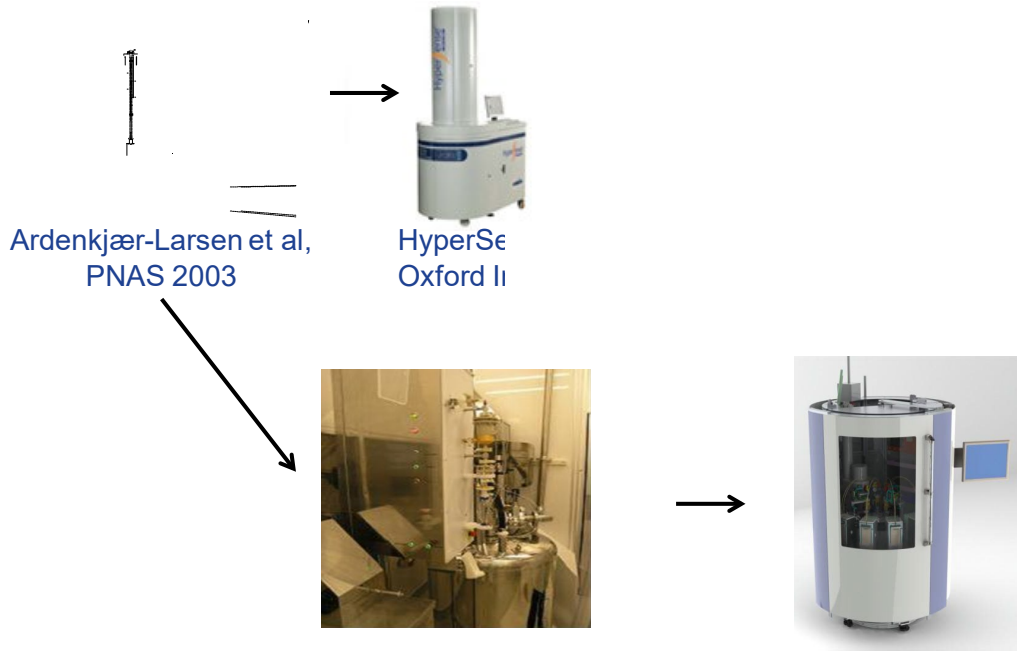

FIG 3

FIG 4

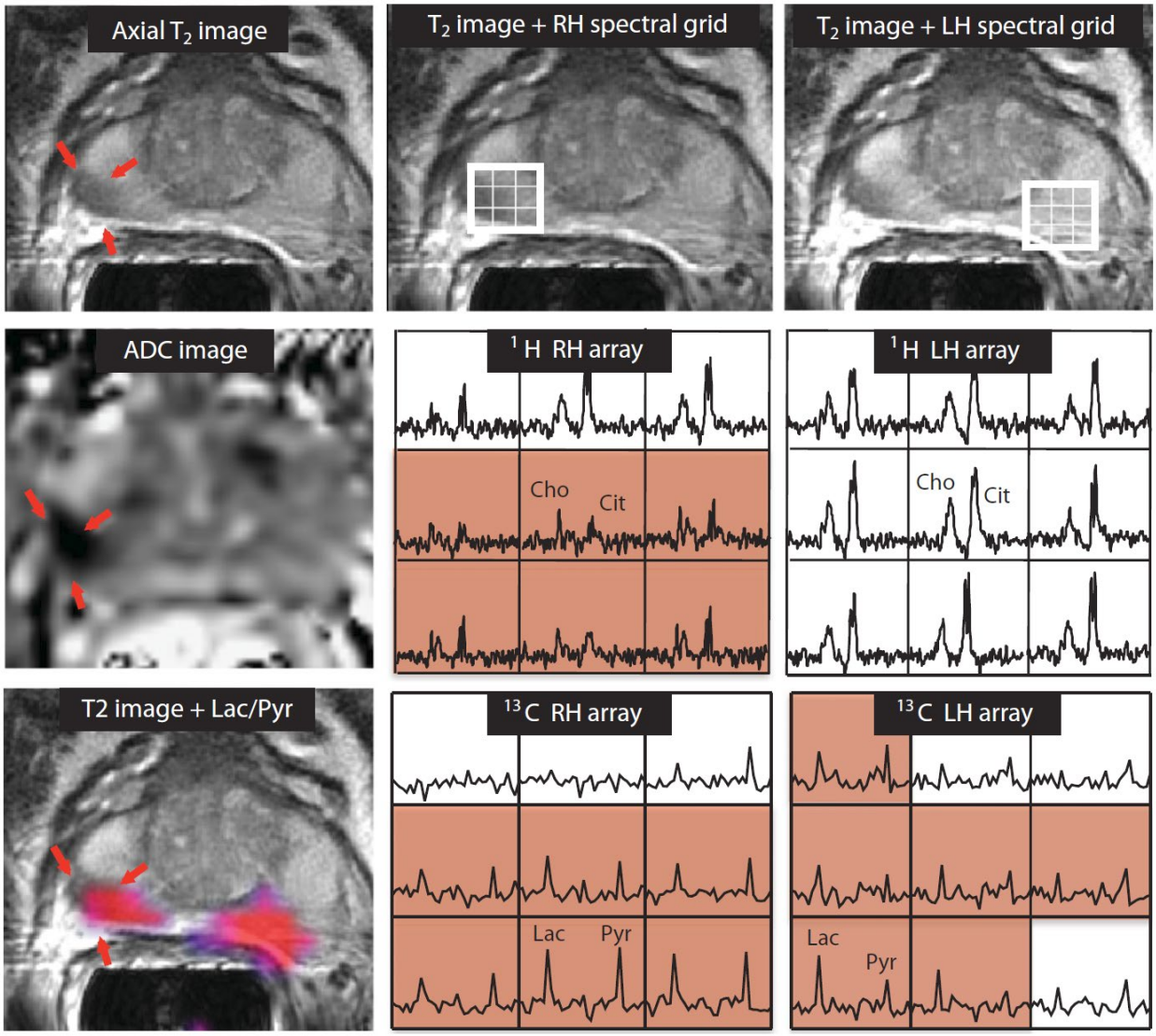
Axial T_2 image
T_2 image + RH spectral grid
T_2 image + LH spectral grid
ADC image
^{1}H RH array
Cho
Cit
^{1}H LH array
Cho
Cit
T2 image + Lac/Pyr
^{13}C RH array
Lac
Pyr
^{13}C LH array
Lac
Pyr

FIG 5:

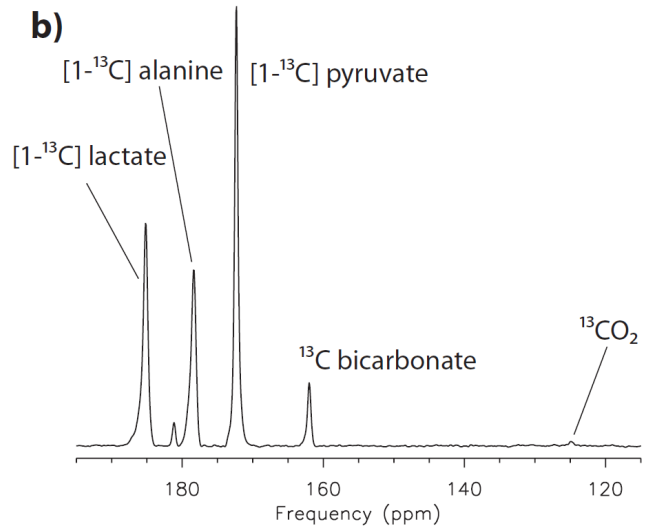
b)
[1-13C] alanine
[1-13C] pyruvate
[1-13C] lactate
13C bicarbonate
13CO2
180
160
140
120
Frequency (ppm)

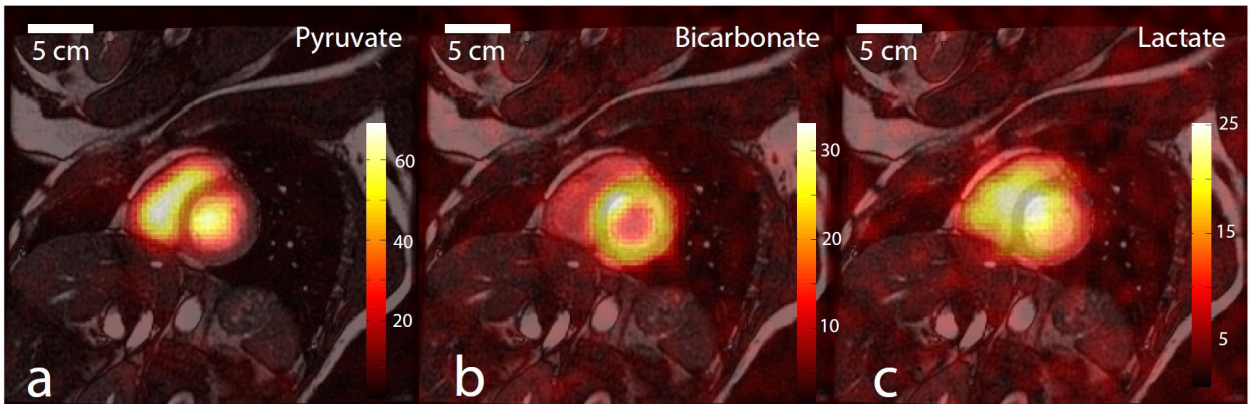
5 cm
Pyruvate
60
40
20
a
5 cm
Bicarbonate
30
20
10
b
5 cm
Lactate
25
15
5
c